Thesis for the degree

Master of Science

Submitted to the Scientific Council of the

Weizmann Institute of Science

Rehovot, Israel

עבודת גמר (תזה) לתואר

מוסמך למדעים

מוגשת למועצה המדעית של

מכון ויצמן למדע

רחובות, ישראל

By

Orr Barnea

מאת

אור ברנע

Dark-Ion-based Pressure and Electric-Field Sensors in a Linear Paul Trap

מדי לחץ ושדה חשמלי מבוססי יונים אפלים במלכודת פול לינארית

Advisor:

Ziv Meir

מנחה:

זיו מאיר

August 2025

אוגוסט תשפ"ה

Abstract

Trapped ions provide a powerful platform for precision measurements and quantum control of both atomic and molecular ions. In this work we present the development of a room temperature linear Paul trap for $^{40}Ca^{+}$ ions, designed to enable precise measurements of mixed crystals of Ca^{+} and N_2^{+} ions and molecular ions, respectively. Toward this goal, two diagnostic techniques are demonstrated, both utilizing the properties and dynamics of mixed-species ion crystals composed of "bright" (fluorescing) and "dark" (non-fluorescing) ions.

First, a pressure gauge based on the reordering rate of a dark ion embedded in a bright-ion crystal was implemented. This method allows direct pressure estimation at the ions' location, and potentially overcoming the limitations of standard ultra-high vacuum (UHV) gauges at pressures below 1×10^{-11} mbar. Using this technique, the final system pressure was estimated to be 2.8×10^{-11} mbar by extrapolating external UHV gauge reading at higher pressure values.

Second, a novel method for detecting and compensating excess micromotion (EMM) was developed (Barnea et al., Front. Quantum Sci. Technol. 4, 1596801 (2025) [1]). By observing the axial deformation of a bright-dark-bright crystal under an applied radial electric field, this field strength could be inferred and nullified. The method's sensitivity was significantly enhanced by operating just above the crystal's transition to zig-zag configuration, and the results were corroborated via comparison with a modified single-ion displacement technique.

These tools highlight the utility of multi-species Coulomb crystals for real-time diagnostics in ion traps and lay the groundwork for future experiments using both atomic and molecular ions.

1 Acknowledgments

The work presented in this thesis could not have been accomplished without the help of multiple people, all of whom I am extremely grateful to. The efforts of Idan Hochner, Jonas Drotleff and Dror Einav have been instrumental to this project, both their work on the trap itself and their advice and encouragement throughout. I am equally thankful for their help and their friendship, along with that of the rest of my lab-mates over the last two and a half years: Mai Faibish, Tom Shahaf, Rukmini Harale, Noga Saban and Evgenii Kipiatkov. This is doubly true for our supervisor Dr. Ziv Meir, whose patience and endless enthusiasm for physics have been truly inspirational. I would also like to thank my family for instilling in me my love of science, and their endless support along the way.

Contents

2 Introduction

Ion traps are a well established platform for studying the internal structure of atomic and molecular ions. They offer a high degree of control over the internal and motional quantum states of the trapped ions and have been proven useful for a wide range of applications, such as precision spectroscopy [2] and optical atomic clocks [3], as well as being a promising avenue for the development of quantum computers [4, 5].

The prospect of utilizing two simultaneously co-trapped ion species has received significant and rising attention in recent years. Multi-species crystals allow for the sympathetic cooling of non-fluorescing ions [6, 7], facilitate the use of quantum-logic-spectroscopy techniques [6, 8–10], and allow for new sensing techniques unavailable for homogeneous crystals [1, 11]. The presence of ions with different properties greatly enrich the behavior of the system, and allow for new dynamics to be studied and manipulated.

The reliability and precision of experiments with ions rely on the minimization of external perturbations. One significant source of such noise arises from collisions with residual background gasses. These collisions can excite the ions' motional modes and can even knock them out of the trap entirely [12]. In addition, state and chemical changing collision can reduce the experimental duty cycle [8], making extremely low ambient pressures necessary for high-fidelity experiments.

A standard technique to measure the ultra-high-vacuum (UHV) condition is to use a commercial UHV gauge. However, when the pressure reaches below 1×10^{-11} mbar, at the lower end of the ultra-high vacuum (UHV) regime, the reliability of standard UHV pressure gauges sharply degrades. Their readings become increasingly uncertain and position dependent, requiring us to find alternative methods for pressure estimation. One such method is to use the collision rate itself as an indicator for the pressure. The rate of reordering events in a mixed-species Coulomb crystal is used to evaluate the collision rate, utilizing the distinguishability of dark and bright ions [11]. This method both has a lower pressure limit and measures the pressure directly at the ions', rather than the gauges, location.

An additional source of background noise is the presence of stray electric fields at the location of the ion. In radio-frequency (RF) Paul traps, such fields displace the equilibrium ion position from the RF null, resulting in additional motion driven by the oscillating trapping fields. This so-called "excess micromotion" (EMM) create signifcant Doppler shifts, and hence must be minimized when conducting precision measurements [13]. While many methods were developed to detect and compensate for the EMM [13–16], many of them require either the direct characterization and manipulation of the ions' energy levels (such as the resolved-sideband method [14]) or the implementation of additional ion

imaging techniques (such as mechanical focus-scanning [15]), keeping them from being implemented in the early stages of the traps development. Additionally, most known compensation techniques utilize only a single ion species, and haven't been expanded to suit a multi-species system.

In this thesis, I present the implementation of two techniques which utilize multi-species crystals in a room temperature ion trap. First, the shape and features of the trap are explained, with the various experimental techniques and processes used to minimize the pressure being described in detail. Second, the development and calibration of a dark-ion pressure gauge is showcased, with the gauge being used to estimate the final pressure of the system to be $\sim 2.8 \times 10^{-11}$ mbar. Finally, an entirely novel method for the detection and compensation of radial EMM using a dark ion is introduced and demonstrated [1]. The method's sensitivity is significantly enhanced using careful tuning of the confining frequencies close to the transition to zig-zag configuration of the multi-specie ion crystal. The results of the compensation are corroborated via comparison to a modified ion-displacement method using a single bright ion.

3 Goals

The overarching goal of my masters was the construction of an experimental apparatus for the trapping, cooling and imaging of $^{40}Ca^{+}$ ions using a linear Paul trap. This setup would serve as a foundation toward achieving quantum control over the internal and motional states of co-trapped atomic and molecular ions [17]. This level of control over the quantum states is expected to allow for high-precision spectroscopy as well as the probing of new physics [18, 19].

The process of building the trap required assembling the trapping chamber itself, the laser lines for ionization and cooling of the ions, the RF and DC electrical fields for confining the ions, as well as an imaging system to detect the position of the ions (Chaper 6). As I did not work directly on the laser lines and the trapping fields themselves, they are only briefly touched upon in this thesis so as to provide details on the experimental system.

A significant focus was put on achieving the extremely high vacuum necessary for performing experiments with molecular ions (Chapter 5). This required reaching pressures of order 10^{-11} mbar. To characterize the vacuum level, a dark-ion shuffling pressure gauge was realized [11]. This gauge uses the frequency of visible reordering events of a dark-ion embedded in a bright-ion crystal to measure the pressure in the trapping chamber. Using this technique, we estimate the final vacuum to be approximately 2.8×10^{-11} mbar (Chapter 7).

During the implementation of the pressure gauge, an unexpected inconsistency in the length of the coulomb crystals was detected. This was theorized to be the result of stray radial electric fields, which affect ions with different mass-to-charge ratios differently, creating a noticeable distortion in the crystal. This insight gave rise to the idea of using the distortion to measure the intensity of the fields, leading to the development of a novel micromotion compensation scheme (Chapter 8). We published a paper on this subject [1], which details and compares two compensation methods: one using a single $^{40}Ca^{+}$ and the other being the aforementioned new "dark-ion" method which uses two $^{40}Ca^{+}$ ions with an additional non-fluorescing $^{44}Ca^{+}$ ion.

4 Theoretical Background

4.1 Linear Paul Traps

It was first proven by Earnshaw that a point charge cannot be confined using static electric fields alone [20]. As such, linear Paul traps use a combination of stationary and oscillating (RF) fields to create an effective trapping potential [21]. The RF potential confines the ions radially, while stationary potentials both confine the ions along the axis of the trap (denoted as the $\hat{z}$ axis) and break the symmetry of the two radial modes:

$$\Phi_{\mathrm{RF}} = \frac{1}{2} V_{\mathrm{RF}} \cos(\Omega_{\mathrm{RF}} t) \left(1 + \frac{x^2 - y^2}{R^2}\right), \tag{1}$$

$$\Phi_{\mathrm{DC}} = \frac{1}{2} V_{\mathrm{g}} \left(1 - \frac{x^2 - y^2}{R^2}\right) + \frac{V_{\mathrm{DC}} - V_g}{z_0^2} \left(z^2 - \frac{1}{2}(x^2 + y^2)\right). \tag{2}$$

Here, V_{RF} (V_{DC}) is the amplitude of the oscillating (stationary) confining fields, V_g is the bias field which differentiates between the radial modes, Ω_{RF} is the frequency of the oscillating fields, and R and z_0 are the characteristic trap dimensions. The form of Eq. 2 emphasizes that for $V_{\mathrm{g}} = V_{\mathrm{DC}}$ we get no axial trapping at all. However, typically $V_{\mathrm{DC}} \gg V_{\mathrm{g}}$ in our experiment. The trap electrode design can be seen in Fig. 6 in chapter 6.

Along the $\hat{z}$ axis the ion behaves as a simple harmonic oscillator with frequency:

$$\omega_{ax} = \sqrt{\frac{2Q(V_{\mathrm{DC}} - V_{\mathrm{g}})}{m z_0^2}}, \tag{3}$$

where m and Q are the ion mass and charge respectively.

In the radial direction, the dynamics are governed by the Mathieu equations:

$$\frac{d^2\bar{x}_i}{d\zeta^2} + [\bar{a}_i + 2\bar{q}_i \cos(2\zeta)]\bar{x}_i = 0, \tag{4}$$

where $i = 1, 2$ denotes the two radial directions and using the definitions:

$$\zeta = \frac{\Omega_{RF}}{2}t, \tag{5}$$

$$a_x = -\frac{4Q}{m\Omega_{\text{RF}}^2}\left(\frac{V_{\text{DC}} - V_{\text{g}}}{z_0^2} + \frac{V_{\text{g}}}{R^2}\right), \tag{6}$$

$$a_y = -\frac{4Q}{m\Omega_{\text{RF}}^2}\left(\frac{V_{\text{DC}} - V_{\text{g}}}{z_0^2} - \frac{V_{\text{g}}}{R^2}\right), \tag{7}$$

and

$$q_x = -q_y = \frac{2QV_{\text{RF}}}{mR^2\Omega_{\text{RF}}^2}. \tag{8}$$

In a typical system we have $|a_i| \ll |q_i| \ll 1$, which yields the approximate solution [22]:

$$x(t) = A_x \cos(\omega_x t)\left[1 + \frac{q_x}{2}\cos(\Omega_{\text{RF}}t)\right], \tag{9}$$

where

$$\beta_x = \sqrt{a_x + \frac{1}{2}q_x^2}, \tag{10}$$

$$\omega_x = \frac{1}{2}\beta_x\Omega_{\text{RF}}. \tag{11}$$

The solution is analogous in the $\hat{y}$ and $\hat{z}$ axes, with $q_z = 0$. The motion can be separated into the large and slow secular motion and the rapid and small micromotion. These terms can be intuitively understood as the secular motion being the effective trapping of the ions and the micromotion describing their response to the time dependence of the trapping field. From Eqs. 6- 8 it is clear that only V_g breaks the radial symmetry of the trap, giving rise to the high and low radial modes, denoted as ω_h and ω_l respectively.

4.2 Doppler Cooling and Fluorescence

The electronic structure of a trapped ion can be approximated by a two-level system, whose Hamiltonian is [22]:

$$\mathcal{H} = \frac{1}{2}\hbar\omega_0(|e\rangle\langle e| - |g\rangle\langle g|). \tag{12}$$

where $|g\rangle$ and $|e\rangle$ are the electronic ground and excited states and ω_0 the transition frequency between them. When a laser tuned near ω_0 is directed at the ion, it can absorb a photon and transition from the

$|g\rangle$ state to the $|e\rangle$ state. The excited electron will eventually decay back to the ground state, emitting a photon either in the direction of the laser via stimulated emission, or in a random direction due to spontaneous emission. Here, we are interested in the latter, as it can be used for imaging and cooling. When spontaneous emission returns the ion to the initial ground state a closed loop is created, enabling repeated absorption and emission cycles. Such transitions are known as cycling transitions, and they form the basis for Doppler cooling and fluorescent detection of ions.

If a camera is placed focusing on an ion with a laser cycling transition, some of the spontaneously emitted photons will end up propagating in its direction and being recorded. For systems with sufficiently short-lived excited state, the absorption-emission cycle can repeat tens of millions of times per second, such that even a lens occupying only a small solid angle can be enough to detect the ion, in what is known as fluorescent imaging.

In practice, the level structure of Ca^+ ions is more complex than just two levels, necessitating the use of additional lasers in order to properly cool the ions (see Fig. 8b). The cycling transition used for fluorescence is between the $4^2S_{1/2}$ (ground) and the $4^2P_{1/2}$ (excited) states, but the excited state can also spontaneously decay to the metastable $3^2D_{3/2}$ state. While the electron is the metastable state the fluorescence is effectively paused, so a "repump" laser is used to excite it back into the loop. Since the excited state is over 15 times more likely to decay into the ground state than the metastable [23] the additional state rarely comes into play, and we can continue to use the two-level system as a reasonable approximation as long as the transition from the metastable state is weakly lased. This can be easily ensured by reducing the detuning the "repump" laser so that the detected fluorescence is maximized.

When a near resonant laser is shined on the two level system, the probability of finding the ion in the excited state is:

$$\rho_{ee} = \frac{s/2}{1 + s + 2\delta_{eff}/\Gamma}, \tag{13}$$

where the saturation parameter s is defined as:

$$s = \frac{2|\Omega|^2}{\Gamma^2}, \tag{14}$$

Ω is the Rabi frequency of the resonant transition, Γ is the decay rate, and δ_{eff} is the effective detuning of the laser. The effective detuning is determined both by the difference in frequency between the laser and the resonance and by the Doppler shift:

$$\delta_{eff} = \omega - \omega_0 - \bar{k} \cdot \bar{v} \equiv \Delta - \bar{k} \cdot \bar{v}, \tag{15}$$

where ω is the laser frequency, $\bar{k}$ the laser momentum, and $\bar{v}$ the atom velocity.

Whenever a photon is absorbed or emitted, the atom receives a momentum kick of $\Delta p = \hbar k$. For stimulated emission, the two kicks cancel each other out, for a total momentum change of 0. In contrast, the kick from a spontaneous emission is in a random direction, so after many cycles the emission kicks average out to 0, leaving a net momentum gain in the direction of the laser. By detuning the laser frequency to be slightly below resonance (red detuning), ions moving toward are preferentially excited, reducing their velocity and leading to a net cooling of the system known as Doppler cooling. The average change in momentum can be attributed to a force called the "scattering force", which for small velocities can be linearized as [24]:

$$F \approx F_s(1 + \kappa v) \tag{16}$$

with

$$F_s = \hbar k \Gamma \frac{s/2}{1 + s + (2\delta_0/\Gamma)^2} \tag{17}$$

shifting the equilibrium position of the ion, δ_0 being the detuning, and the effective friction coefficient being given by:

$$\kappa = \frac{8k\delta/\Gamma^2}{1 + s + (2\delta/\Gamma)^2} \tag{18}$$

This cooling process can continue until it reaches the Doppler limit, which is given by [22]:

$$T_{min} = \frac{\hbar\Gamma\sqrt{1+s}}{4k_B}(1 + \xi), \tag{19}$$

where $\xi = 2/5$ is a geometric factor related to the directionality of the spontaneous emissions.

For our case of the $S_{1/2} \rightarrow P_{1/2}$ transition in $^{40}Ca^+$, we expect a lower bound of ~ 0.39 mK in the limiting case of $s \ll 1$. As long as the laser direction isn't perpendicular to any of the normal modes of the ion's motion, we are able to reach the Doppler cooling limit using only a single laser.

When multiple ion species are co-trapped simultaneously, the motional eigenstates become shared between the entire crystal. This allows ions with accessible cycling transitions to cool ions without direct laser cooling, a phenomenon called sympathetic cooling. Ions who aren't Doppler cooled will also not fluoresce but remain invisible, giving rise to the terms "bright" and "dark" ions respectively. When imaged by a camera, dark ions appear as "holes" within bright ion crystals.

4.3 Coulomb Crystals

To describe the structure of multiple trapped and cooled ions, we can neglect the inherent micromotion and treat the ions as confined in a three-dimensional harmonic potential [21]:

$$\Phi = \frac{1}{2}m[\omega_x^2 x^2 + \omega_y^2 y^2 + \omega_{ax}^2 z^2]. \tag{20}$$

where m is the ion mass, ω_{ax} is the axial secular trap frequency (Eq. 3) and $\omega_{x,y}$ are the radial secular frequencies (Eq.11).

When N identical ions are trapped simultaneously, their Coulomb interaction will repel them from the trap center. If the radial confinement is sufficiently strong, the ions will settle into a $1D$ chain along the axial $(\hat{z})$ direction, forming a linear crystal. The equilibrium positions of the ions minimize the total potential energy, leading to unequal spacings between them [25]:

$$U = U_{trap} + U_{int}, \tag{21}$$

where,

$$U_{trap} = \frac{1}{2}\sum_{i=1}^{N} m_i(\omega_{i,x}^2 x_i^2 + \omega_{i,y}^2 y_i^2 + \omega_{i,ax}^2 z_i^2), \tag{22}$$

and

$$U_{int} = \frac{Q^2}{4\pi\epsilon_0}\sum_{\substack{i,j=1\\ i<j}}^{N} \frac{1}{|\bar{r}_i - \bar{r}_j|}, \tag{23}$$

where ϵ_0 is the vacuum permittivity, and $\bar{r}_i$ is the position of the i^{th} ion.

When either the axial potential or the number of ions N is increased beyond a critical value, the 1D chain will break into a zigzag pattern that reduces the axial contribution to the potential at the expense of the radial trapping.

Realistically, trapped ions are also influenced by stray external electric fields, which are typically slowly varying and nearly uniform on the scale of the crystal. These fields lead to residual motion of the ions driven by the RF fields, known as excess micromotion (EMM). It is typically desired in ion trapping setups that this motion be reduced as much as possible.

Adding a constant external electric field $\bar{E}$ modifies the trapping potential:

$$U_1 = \sum_{n=x,y,z} \frac{m\omega_n^2}{2} r_n^2 + \bar{E}\cdot\bar{r}, \tag{24}$$

which can be rewritten as:

$$U_1 = \sum_{n=x,y,z} \frac{m\omega_n^2}{2}\left(r_n + \frac{E_n}{m\omega_n^2}\right)^2 - \frac{E_n^2}{2m\omega_n^2}. \tag{25}$$

Thus for a crystal of identical ions the primary effect of the stray field is a uniform shift of the entire crystal. However, when considering multi co-trapped species of ions this is no longer the case. Recalling the expressions for the axial and radial trapping frequencies (section 4.1), we see that they are mass dependent:

$$\omega_{ax} = \frac{\Omega_T}{2}\sqrt{a_z}, \tag{26}$$

$$\omega_{x,y} = \frac{\Omega_T}{2}\sqrt{a_{x,y} + \frac{q_{x,y}^2}{2}}, \tag{27}$$

with

$$a_i, q_i \propto \frac{1}{m}. \tag{28}$$

Since the potential depends on the term $m\omega_n^2$, the axial potential term is mass-independent, while the radial is not. Hence a crystal with mixed ion species will acquire a differential shift due to external radial electric fields, causing a deformation of the crystal (see Fig. 1).

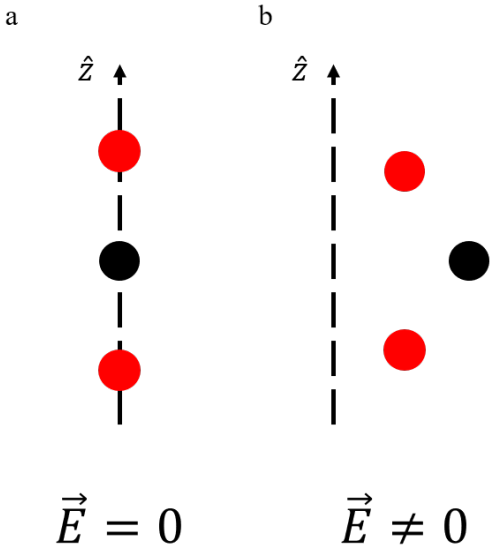

Figure 1: Illustration of the differential shift acquired by different ion species due to uncompensated EMM in a bright-dark-bright configuration crystal. a) When no external fields are present, all the ions are found along the axial axis at the center of the trap, which is marked by the $\hat{z}$ axis. b) When external radial fields are introduced, the different masses of the ions cause them to be differently displaced from the trap's axial center (here black ion's mass is larger than red's ion mass). The increased radial distance between the red and black ions decreases the Coulomb interaction between them, causing the red ions to shift closer to each other.

5 Achieving Ultra High Vacuum

A necessary condition for any experiment involving trapped ions is achieving sufficiently low pressure within the trapping chamber. High pressure can limit ion cooling and lead to frequent collisions that eject ions from the trap or lead to a chemical reaction necessitating loading new ions to the trap. This leads to reduction in experimental duty cycle and limits the ultimate precision of the experiment. While extreme low pressures are achieved with cryogenic systems, our goal is to arrive at ultra high vacuum (UHV) at room temperature which is sufficient to perform our first experiments.

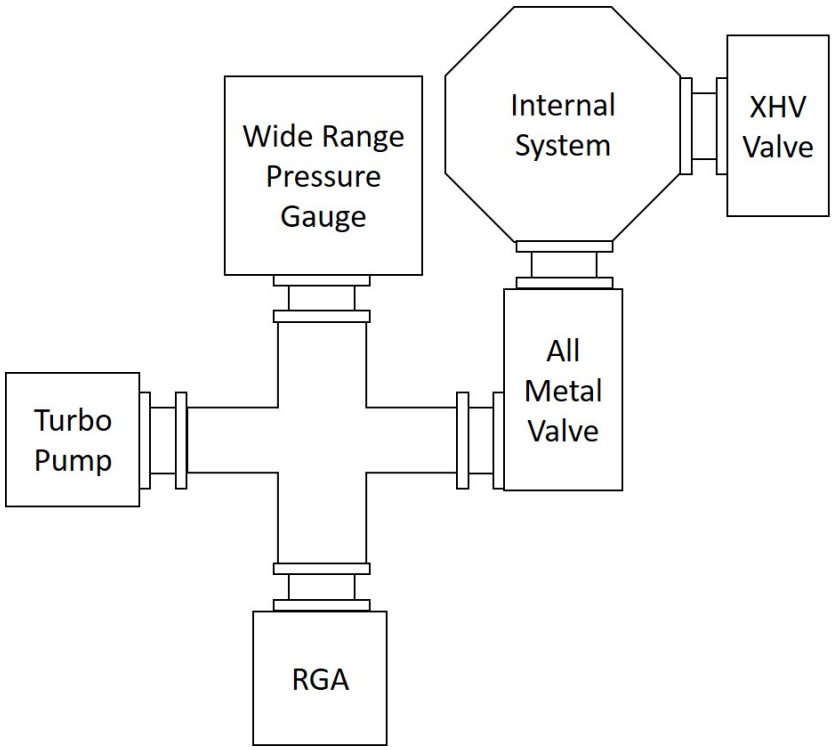

Figure 2: Schematic diagram of the external subsystem of the vacuum setup connected to the ion-trap vacuum chamber (internal system). The Residual gas analyzer (RGA) was replaced with a N_2 valve and feedthrough during venting (see section 5.2)

5.1 Vacuum System Overview

The vacuum setup is composed of two interconnected subsystems, separated by an all-metal angle valve: an internal system containing the trap chamber itself, and an external system which was used during the construction of the internal system and later removed (see Fig. 2). The two subsystems are joined during bake-out, leak testing, and the degassing of the UHV pump, and are separated (using the all-metal angle valve) afterward to achieve the final vacuum in the trap chamber. This design provides operational flexibility: it allows components in the external system to be exchanged or modified without exposing the trap chamber to air, thus avoiding the need for additional bake-outs (see section 5.2).

The trap chamber is pumped by a Nextorr Z-2000 UHV pump, and includes the core experimental components: the ion trap itself, an oven to load the calcium ions, an ultra-high vacuum gauge, viewports for laser access and imaging, and electric feedthroughs for trap operation. The chamber is attached to two valves: the all-metal angle valve connecting to the external subsystem, and a gate valve that will connect to a molecular beam machine in future experiments.

Since the UHV pump works by chemically trapping background gasses, it saturates rapidly if

exposed to air. Therefore, an additional pump is needed to remove gases during pump-down and system preparation, preventing premature saturation of the UHV pump. This role was fulfilled by a Leybold Turbolab 450 Turbomolecular pump, which pumps the external parts of the system. The external subsystem also housed a wide-range pressure gauge and a residual gas analyzer (RGA) used for leak testing.

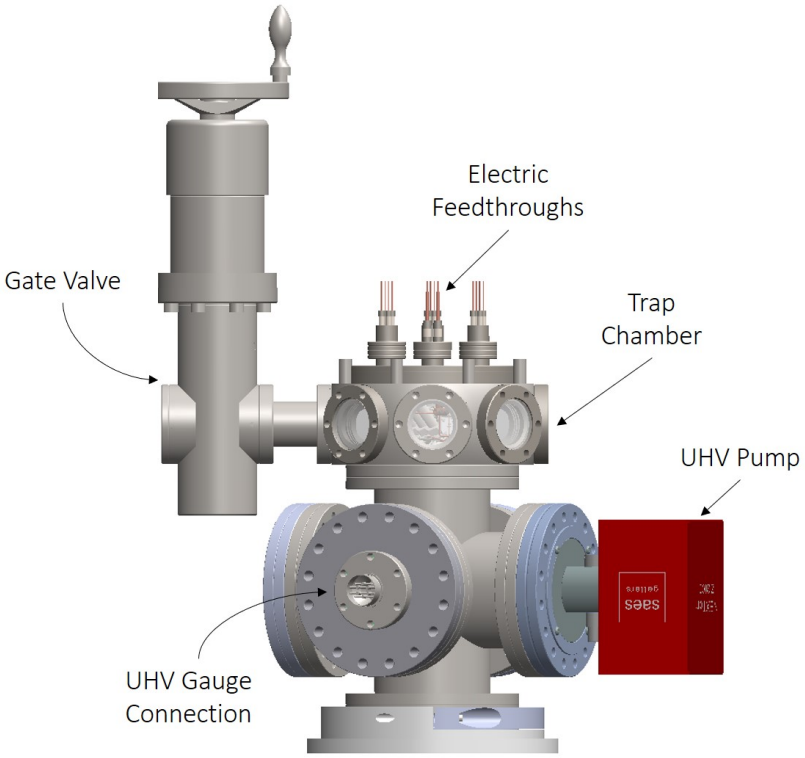

Figure 3: The ion-trap vacuum chamber and internal subsystem. The all-metal angle valve connecting the external and internal systems was placed opposite to the UHV gauge and is not shown in this figure.

5.2 Degassing the System

The final pressure of a vacuum system is determined by the balance between its pumping capacity and the combined rates of leaks and out-gassing. In order to arrive at the lowest achievable pressure, it is essential to minimize leaks and remove trapped gases from the materials composing the system. To this end, several experimental procedures were developed and implemented to prepare the system while avoiding damage to sensitive components. The most important procedures, along with their underlying rationales, are described in the following subsections.

5.2.1 Air-Baking

Outgassing—the diffusion of gases from materials into the vacuum—poses a major challenge to achieving ultra-high vacuum at room temperature. While materials will eventually outgas naturally when placed in vacuum, the process can take weeks or months. In order to deplete the amount of hydrogen molecules in the bulk of the material, the trap chamber and attached flanges were first air-baked at $400\,^{\circ}\mathrm{C}$ overnight [26] in an oven. This process differs from the following bake-out procedure due to being preformed at atmospheric pressures.

5.2.2 Bake-Out

The main technique used to lower the system's out-gassing rate was a vacuum bake-out, in which the assembled system was heated using heating cables while in vacuum for an extended period. During bake-out, the trap chamber was pumped by the external turbomolecular pump, allowing gases released from materials to be continuously removed from the system. Heating was done gradually, in increments of $10 - 20\,^{\circ}\mathrm{C}$ up to a maximum of $180\,^{\circ}\mathrm{C}$, in order to avoid thermal shocks to the system. To avoid strong temperature gradients that could cause mechanical deformation and leaks, the system was wrapped in multiple layers of aluminum foil both under and over the heating cables. The outer aluminum layers were loosely wrapped around the system so as to trap a layer of air, increasing thermal insulation and preventing heat loss. A typical temperature-pressure (TP) curve of a bake-out process is shown in Fig.4.

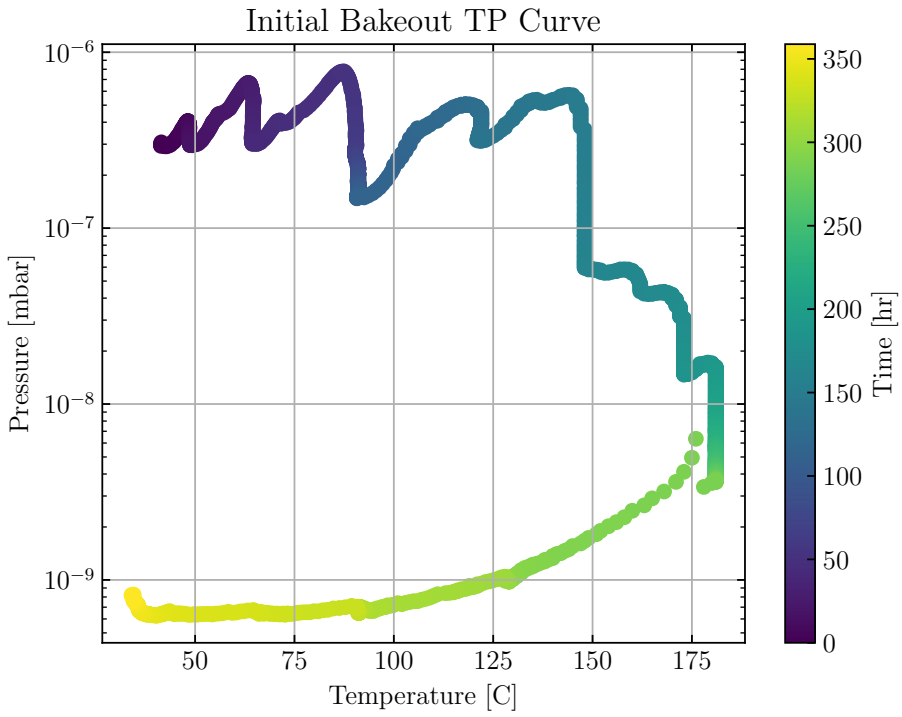

Figure 4: TP curve of the initial bake-out process. The temperature is modified in staggered steps, with the pressure being allowed to settle between steps.

5.2.3 Degassing of the UHV Pump

Once the bake-out was complete, the final preparation step was the degassing of the UHV pump to maximize its pumping efficiency. This must be done after the bake-out has concluded to avoid re-saturating the UHV pump with the increased out-gassing during bake-out. The pump is composed of two parts, each pumping different gasses and must be operated and degassed separately.

- **Sputter-ion pump**: Quickly degassed by cycling the pump on and off repeatedly.
- **Non-evaporable getter (NEG)**: Requires Requires thermal activation by heating to over 450 °C for at least an hour.

Direct activation of the NEG causes the body of the trap apparatus to heat up rapidly, creating dangerous thermal gradients that may cause leaks. To prevent this, the NEG is first conditioned at medium temperatures of 200 °C and 300 °C, allowing the system's temperature to stabilize in two steps before increasing it further.

5.2.4 Leak Testing

Leaks introduce a continuous influx of background gas, setting a hard limit on the minimal pressure achievable. To identify and locate leaks, a residual gas analyzer (RGA) was used to monitor the partial pressure of helium. Helium gas was sprayed systematically over the system's flanges and joints. Leaks were detected as sharp increases in the helium signal directly following such sprays.

5.2.5 Nitrogen Venting

The oven in the trapping chamber is filled with calcium grains (see 6.2), which quickly oxidize when exposed to air. To prevent this, any change to the inner parts of the system requires venting it with nitrogen, as was done when the gate valve was attached to the system. Nitrogen venting also has the added benefit of preventing moisture buildup on the inner walls of the system, reducing the time required for bakeout. This was done by replacing the RGA with a feed-through (while the all-metal valve is closed), and then filling the system with N_2 to a pressure of between 1 and 1.5 bar. If the system is opened and closed fast enough, the ambient nitrogen rushing out of the system ensures that the calcium grains remain unoxidized. The integrity of the calcium can be verified by activating the oven and the 422 nm laser and observing the fluorescence of the emerging particle beam, without the need for ionizing and trapping the Ca atoms.

5.3 Bakeout Results

Throughout the construction of the trap, the system underwent a degassing procedure three distinct times. The first degassing was performed on a simplified setup as a systems check for the heating cables and UHV pump. The procedure was enacted on a simplified system consisted of an empty trapping chamber with blanks on all sides, and consisted of a full bake-out, and direct activation of the NEG to a temperature of $550^{\circ}C$, without prior conditioning. The system was then leak-tested, revealing a leak in an improperly fastened screw. Following this discovery, the system was "half baked" to a temperature of $100^{\circ}C$ as a time saving measure. After cooling down, the UHV gauge showed a final pressure of 1.2×10^{-11} mbar, which served as a benchmark for achievable pressures going forward.

The second degassing was performed on a nearly complete system (missing only the gate valve in the internal system) and consisted only of activating the NEG. This was done to reach a pressure on the scale of 1×10^{-10} mbar, low enough to observe trapped ions, without the time investment of a

full bake-out. Initially, the NEG was activated directly with a temperature of $550°C$, similarly to what was done in the first degassing. This however led to a significant leak, as can be seen in Fig. 5.

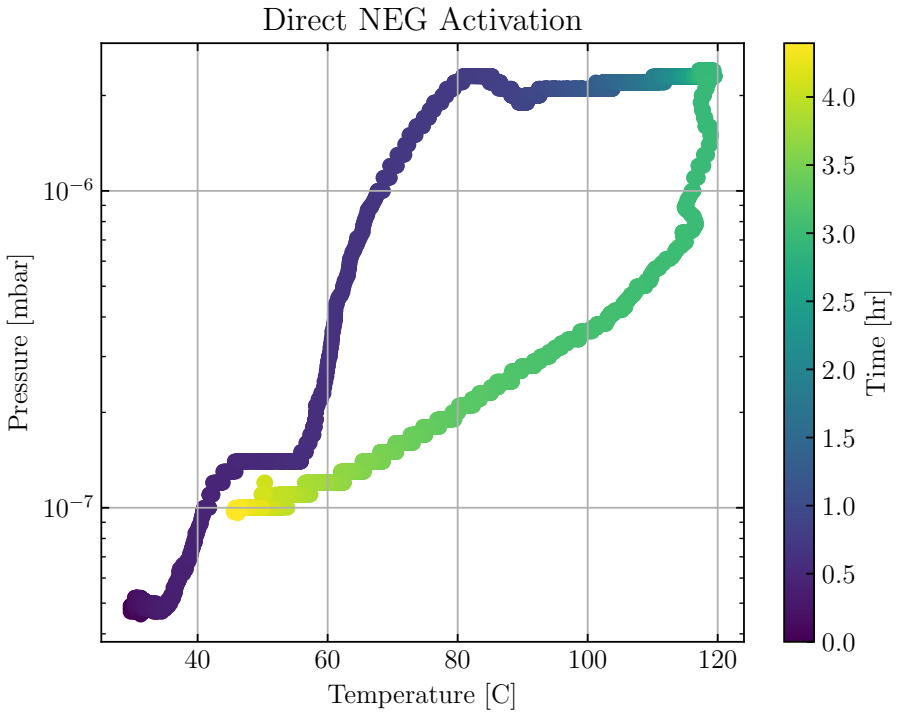

Figure 5: Activation of the UHV pump NEG at $550°C$ from room temperature. The presence of a leak can be seen by the increased pressure due to the activation. Note that this curve was measured by a wide range pressure gauge placed in the external system to avoid activating the UHV gauge in potentially high pressures

After finding and fixing the leak, the NEG was activated again after conditioning it in two steps as described in section 5.2, reaching a final pressure of 3.4×10^{-10} mbar.

The final degassing was done on the full system and included both a full bake-out and NEG activation. In order to smooth the temperature gradients formed along the body of the trap the heating was done by two sets of heating cables which could be adjusted independently, along with small fans to cool down overheated portions. The NEG was conditioned at $300°C$ both before and after the bake-out in order to ensure the de-saturation of the NEG and avoiding leaks. The bake-out took overall approx. 30 days, with 13 of whom spent at the maximum temperature, and leading to the system eventually settling on a final pressure of 1.5×10^{-11} mbar, as measured by the UHV gauge. A summary of the three procedures and their final pressures is presented in table 1.

The final pressure presented above was measured using the UHV gauge, which is naturally less accurate at very low pressures. Additionally, the gauge is placed adjacent to the UHV pump, which could cause it to measure pressures lower than those actually experienced by the ions. Hence we

Degassing Procedure	Dates	Setup Description	Degassing Steps	Final Pressure
1st	13–28/6/23	Simplified	Bake-out, NEG activation	1.2×10^{-11} mbar
2nd	15–16/8/23	Full	NEG conditioning and activation	3.4×10^{-10} mbar
3rd	19/2/24–20/3/24	Full	Bake-out, NEG conditioning and activation	1.5×10^{-11} mbar

Table 1: Summary of degassing procedures used throughout the development of the system

would like a method to measure the pressure using the ions themselves, which would neatly eliminate both of those concerns. The method and results of creating such a gauge are presented in chapter 7.

6 Ion Trap Apparatus

This chapter serves as a brief overview of the experimental subsystems necessary for the ionization, loading, cooling and imaging of the Ca^+ ions.

6.1 Trap Geometry

The core of the ion trapping apparatus is the linear Paul trap itself, which is composed of four segmented titanium blades attached to a ceramic frame. The blades are divided into pairs of opposing electrodes, with one pair being the RF electrodes, and the other being divided into the bias and the DC electrodes. Two tungsten rods were added near the blades to allow for micromotion compensation. An additional tickle rod was used in order to apply additional RF fields on the trap, thereby finding the frequencies of the motional modes of the ions [6]. The construction of the electrodes is shown in Fig. 6. The body of the trap is made of ceramic Shapal^{TM}, which is a vacuum-compatible and nonmagnetic material, with a high thermal conductivity.

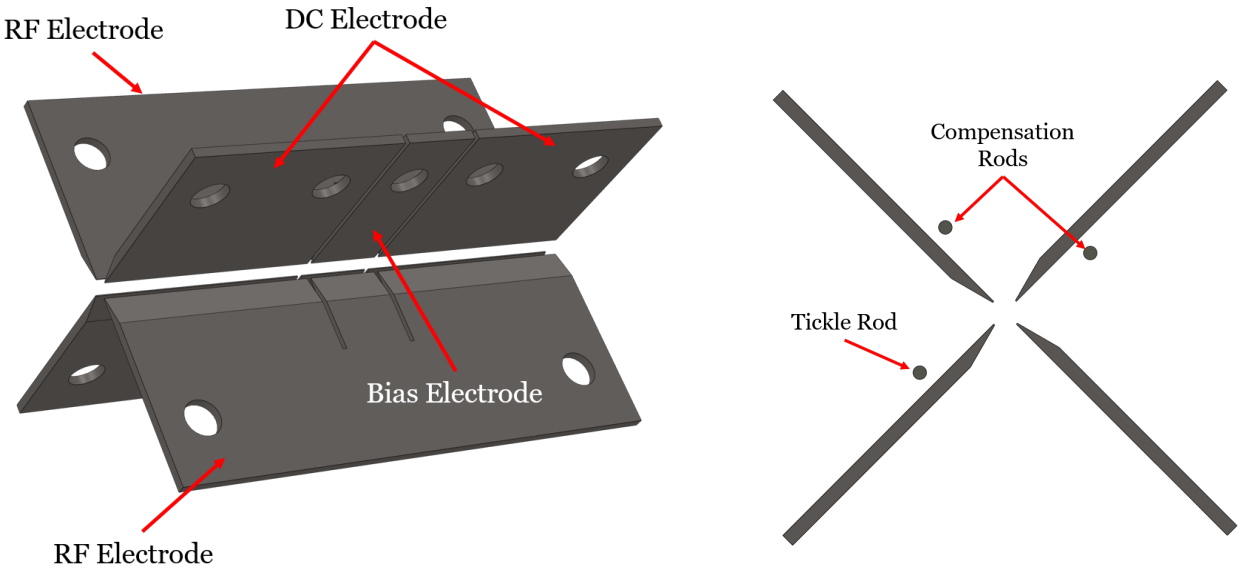

(a) The electrodes of the linear Paul trap. The structure of the DC and Bias electrodes is identical on the other side of the trap. The width of the bias electrodes is 4.1mm, of the DC electrodes is 12mm, and the distance between them is 0.25mm

(b) Side view of the electrodes and compensation rods. The distance between opposing electrodes is 1.2mm

Figure 6: The electrodes of the linear Paul trap, shown from the front (a) and the side (b).

6.2 Ion Loading Mechanism

The calcium atoms were loaded into the trap using a homemade oven filled with pure calcium grains. The oven is made of a titanium tube with stainless steel wires and is connected to a DC power supply. When a current is passed through the oven, the tube is resistively heated increasing the vapor pressure of the calcium and causing a beam of neutral atoms to be ejected toward the trap. These atoms were ionized using a 1+1' resonance-enhanced-ionization scheme, which could be tuned to selectively trap different Ca isotopes (see section 6.4 below).

6.3 Imaging System

The trap was imaged using an Andor Luca S EM-CCD camera and an objective with a working distance of ∼30 mm and focal length of ∼37mm. The magnification was measured using the distance between two bright ions as a ruler, and found to be ∼1.13 µm/pixel. A filter with a transmission window (optical density > 5) of 20nm around 400nm was used to reduce the ambient light while passing almost all of the fluorescence from the bright ions (see subsection 6.4 below). The exposure time was adjusted as needed for different measurements, ranging from 0.1sec for the pressure gauge

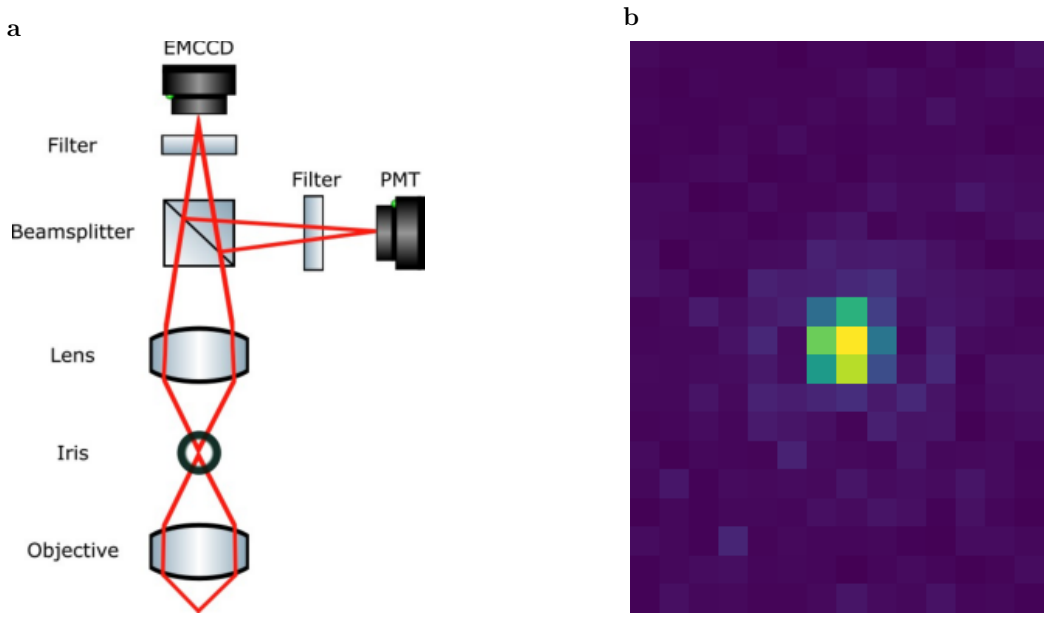

Figure 7: a) Diagram of the imaging system used throughout the experiment. Red lines portray the beam trajectory. An iris was placed on the image plane of the objective in order to reduce background scattering. The ions were then re-imaged on the EMCCD using an additional lens with focal length of 45mm. The beam-splitter and photon-multiplier tube (PMT) shown here were added later on for experiments involving internal energy states manipulation (not part of this thesis). b) A sample image of a $^{40}Ca^{+}$ ion captured by the imaging system.

measurements to 1sec for the EMM compensation measurements. A diagram of the imaging system is shown in Fig.7.

6.4 Laser Lines

The laser lines constructed for the operation of the trap are as follows (see Fig.8):

- **422** nm- Used to excite the ^{40}Ca atoms from the ground state. The reference wavelength was tuned by maximizing the fluorescence from a beam of neutral atoms.
- **375** nm- Used to ionize the atoms already excited by the 422 nm laser as part of the 1+1' ionization scheme. Since it couples a state to the continuum its wavelength was not locked.
- **397** nm- Used for Doppler cooling the ions, as well as being the wavelength of the spontaneous emission detected by the imaging system. Tuned by maximizing the signal from trapped ions.
- **866** nm- Used to re-pump the decay branch from the $4^2P_{1/2}$ state to the $3^2D_{3/2}$ state. Since the decay from the $3^2D_{3/2}$ state to the ground state is forbidden, this laser is necessary to detect any signal from the trapped ions. Its reference wavelength was tuned alongside the 397 nm laser.

All except the 375 nm laser were monitored by a wavelength meter (HighFinesse WSU8-10) which was also used to stabilize their wavelength up to the sub-MHz scale.

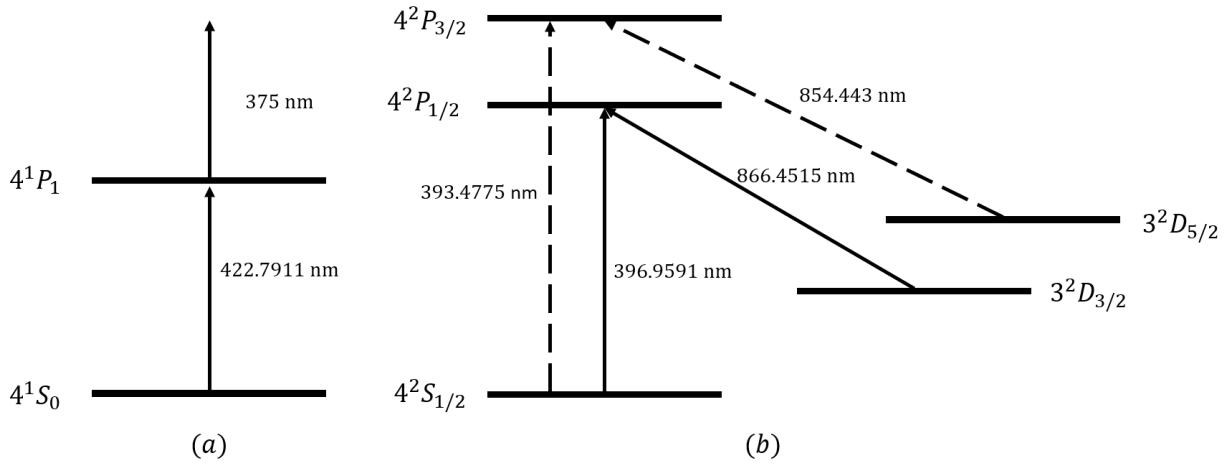

Figure 8: Energy Levels of ^{40}Ca (a) and $^{40}Ca^{+}$ (b) [27]. Solid line transitions were lased in the system. The 375nm laser couples the 4^1P_1 transition to the continuum, ionizing the atom.

Different isotopes of Ca have the same energy level structure, but their energy levels each shift by a non-negligible amount compared to each other [28]. We exploited this phenomenon to selectively ionize and trap the ^{44}Ca isotope by tuning the 422 nm laser accordingly. The isotope shift of the cycling transition is sufficiently large such that the $^{44}Ca^{+}$ ions don't emit light to any measurable degree but are instead sympathetically cooled by their bright neighbors in the crystal [28].

7 Dark-Ion Pressure Gauge

7.1 Collisions in an Ion Trap

The pressure inside the trap chamber affects the trapped Coulomb crystal through collision events between background gas molecules and the trapped ions. For a system with pressure P and temperature T, the mean collision rate per ion with a given molecule is:

$$\gamma = \frac{Pq}{k_B T}\sqrt{\frac{\pi\alpha}{\mu\varepsilon_0}}, \tag{29}$$

where q is the ion charge, α is the molecule's polarizability volume and μ is defined as the reduced mass of the colliding system [11]:

$$\mu = \frac{m_i m_m}{m_i + m_m}, \tag{30}$$

where m_i and m_m are the masses of the ion and molecule respectively.

These collisions can be observed experimentally by co-trapping bright and dark ions and tracking the rate at which their positions interchange. In a crystal with multiple bright or dark ions, only reorderings where a dark ion swaps places with a bright ion will be measurable. Denoting the total number of ions as N, of whom D are dark, the probability of a collision leading to a measurable reshuffling of the crystal (as opposed to an unmeasurable one) is:

$$p(N, D) = 1 - \frac{D!(N - D)!}{N!}, \tag{31}$$

where the factorial terms account for the number of equivalent configurations. This expression assumes that all possible orderings are equally probable following a collision. When accounting for the detection probability, the normalized collision rate per ion is given by:

$$\gamma = \frac{\gamma_{N,D}}{Np(N, D)}. \tag{32}$$

Where $\gamma_{N,D}$ is the measured reordering rate. This normalization is only applicable under the assumption that collisions involving bright and dark ions are equivalent, despite their differing masses. Since the mass difference between the bright $^{40}Ca^{+}$ and the dark $^{44}Ca^{+}$ is only 10%, this is a reasonable assumption, especially for small background gas molecules such as H_2.

7.2 Evaluating the Collision Rate

The time between successive ion-molecule collisions is expected to be memoryless, following an exponential distribution. To measure the collision rate, we trapped dark ions within a bright ion crystal and monitored their positions over time. The positions were determined by operating the EMCCD camera at a frame rate of approximately 10 Hz. For each frame, we averaged the pixel columns around the ion positions and fitted the result to a series of Gaussian profiles. Dark ion positions were identified via ”holes” in the Coulomb crystal (see Fig. 9). Reordering events were identified by comparing the dark ion positions between consecutive frames. The time elapsed between two successive reorderings was recorded and fitted to an exponential distribution function using Bayesian inference, confirming the expected statistical behavior.

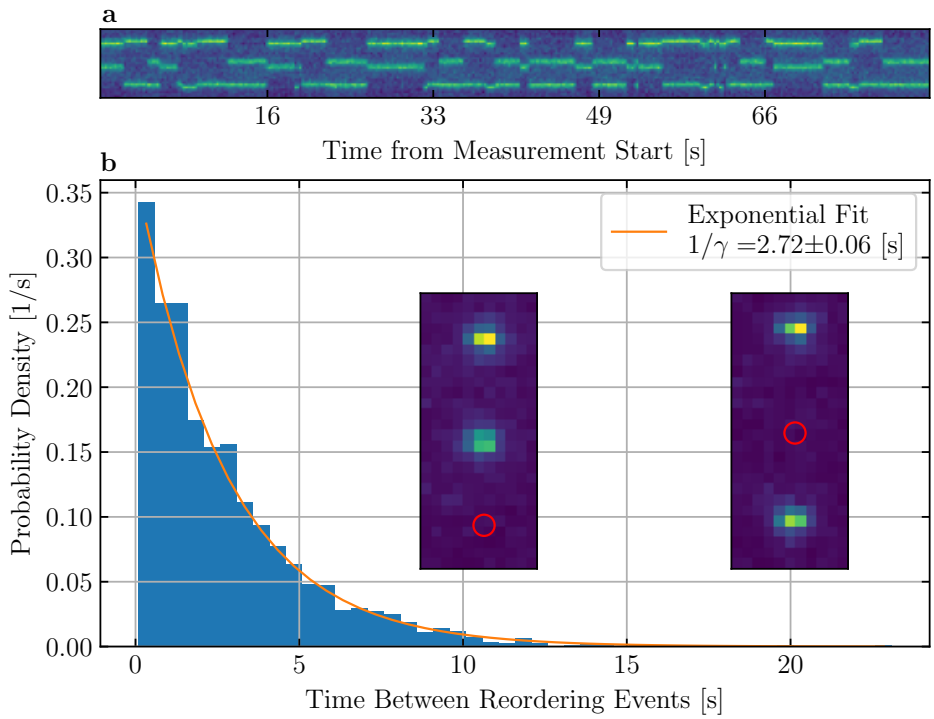

Figure 9: a) Collation of images of the ion positions, each averaged over 3 frames to reduce visual noise. Collisions are recorded when successive frames show the dark ion to be in two different positions within the crystal. The inconsistent positions of the bright ions are due to the crystal being deformed by stray radial electric fields (see chapter 8). b) Histogram of times between successive dark-ion reordering events within the Coulomb crystal, fitted to an exponential distribution. Insets are two distinct configurations of the crystal, averaged over 30 frames and with the dark ion position marked by a red circle.

The jump rate measurements were conducted in three sets.

- The first set was measured before any degassing procedure was implemented on the full setup, so as to serve as a baseline for the calibration (5–19/9/23).
- The second set was measured after the shortened conditioning process, denoted as the second degassing procedure in table 1 (6–7/2/24).
- The third set was recorded after the final bakeout, due to the UHV gauge being expected to be increasingly unreliable when going below 1×10^{-10} mbar. Activating the UHV gauge at this stage was found to cause external fields which interfere with other experiments performed in the setup, so its readings were not recorded (20/8–3/9/24).

A linear calibration curve was established by plotting the measured reordering rate against the UHV gauge readouts from the first two sets. This calibration allowed us to estimate the pressure during

the third set, based on the measured reordering rate. The results of the measurements are shown in Fig. 10, with the final pressure being evaluated to be at approx. 2.8×10^{-11} mbar. It should be noted that the system was physically moved (from a temporary lab to our new lab) before the last set of measurements, which could have somewhat distorted the final results due to the slightly different trapping parameters. The trap RF was set with a frequency of approx. 14.06MHz and voltage between $0.043 - 0.06$V before the move, which was changed to a frequency of 14.84MHz and 0.1V amplitude after. The DC voltage was kept constant at 40V throughout.

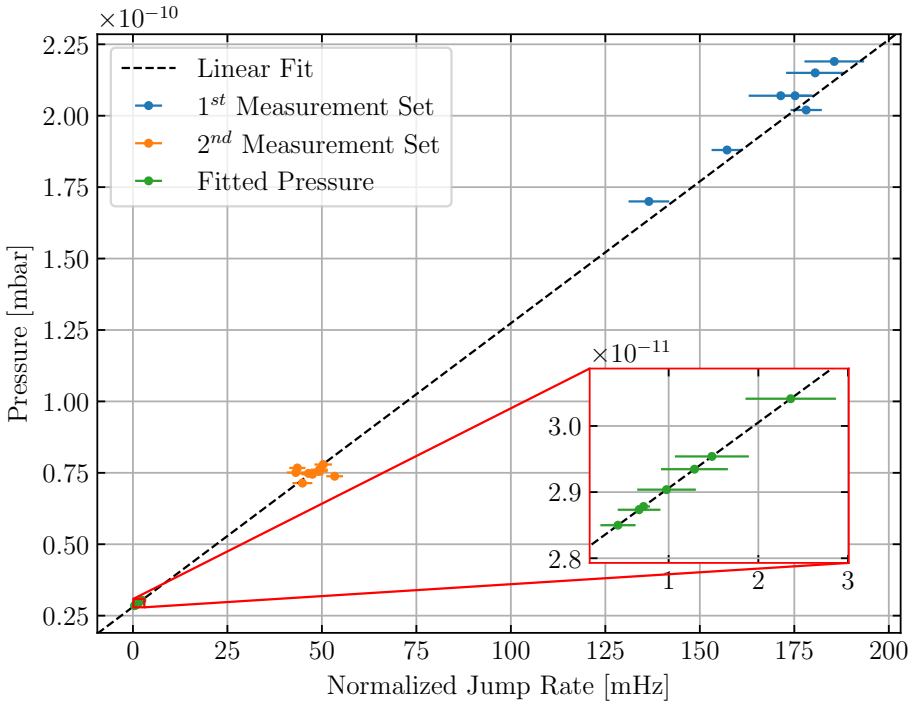

Figure 10: Calibration and results of the dark ion pressure gauge. Only the first two measurement sets (blue and orange) were used to find the linear fit (dashed line), with the UHV gauge being inactive during the third measurement set (green). The error-bars represent the statistical uncertainty of the evaluation of the mean jump rates.

The main advantage of the dark ion pressure gauge over relying on the UHV gauge is that while the UHV gauge is unreliable at very low pressures, the dark ion gauge actually grows more accurate as the vacuum improves. Throughout the experiment, we operated the EMCCD camera at rate of 10 Hz, which defines the limit of our temporal resolution. But as the normalized jump rate decreases to the mHz scale, the error due to the sample rate becomes essentially irrelevant. At such low pressures the main limitation on the gauge accuracy is the long time needed to record statistics on the jump rate.

An additional advantage of the dark ion gauge is that it directly measures the pressure as experienced by the ions, thus eliminating pressure gradients between the UHV gauge position and the

experiment chamber. Since the UHV gauge in our system lies closer to the ion pump than to the trap chamber, this difference is potentially significant.

8 Dark-Ion Electric Field Sensor

8.1 The Dark Ion Compensation Method

As elaborated on in section 4.3, applying a radial electric field to a Coulomb crystal with multiple ion species distorts the structure of the crystal, due to the differing mass-to-charge ratios. When the ions are in a linear configuration, varying the external radial field will cause observable changes in the ions axial positions. We can make use of this phenomenon to detect and compensate for EMM. We use a linear crystal of two bright $^{40}Ca^{+}$ and one dark $^{44}Ca^{+}$ ions, in the bright-dark-bright configuration. An illustration of the experimental setup is shown in Fig. 11. We denote the axes of the radial fields generated by the compensation electrodes as $\hat{V}_{x'}$ and $\hat{V}_{y'}$ to distinguish them from the axes captured by the imaging system: the radial $\hat{x}$ and $\hat{y}$ axes and axial $\hat{z}$ axis.

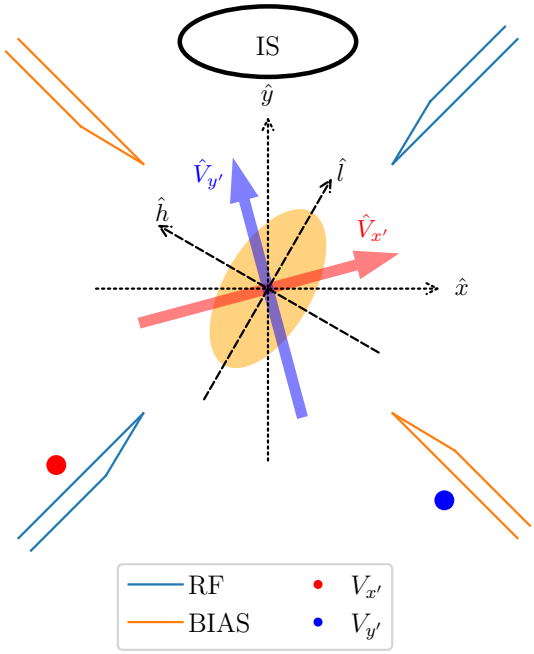

Figure 11: Sketch of a radial cross section of the ion trap showing the RF (light blue) and BIAS (orange) trap electrodes, which control the RF and bias trapping-fields amplitudes. Two compensation rods, $V_{x'}$ (red) and $V_{y'}$ (blue), create a radial electric field along the $\hat{V}_{x'}$ and $\hat{V}_{y'}$ directions. The imaging system (IS) captures the position of the ions along one projection of the radial direction ($\hat{x}$) and the axial direction ($\hat{z}$). The displacement of the ions due to external field is dependent on the orientation (dashed axes) and ratio (orange ellipse) of the high ($\hat{h}$) and low ($\hat{l}$) radial modes.

When the external field is varied, the radial distance between the dark and bright ions changes, causing the axial distance between the bright ions to contract. When the trap is perfectly compensated the dark ion is exactly halfway between the bright ions, and the crystal is at its maximal axial extent. As the radial field increases, the dark ion is pushed further and further away, further decreasing the distance between the bright ions (see Fig. 1). Hence, by finding the compensation voltages where the distance between the bright ions is maximized, we can accurately compensate the trap.

Axial deformation due to radial displacement is quadratic in nature. Hence, we need to enhance the sensitivity of our method further. We do so by working near the transition from a linear to a zig-zag configuration in a bright-dark-bright three-ion crystal [29]. Near the transition, the frequency of the radial bending mode approaches zero (mode softening) [30], significantly enhancing crystal deformation for a given stray field. Below the transition frequency to zig-zag configuration, the dark ion no longer passes through the center of the crystal when when the radial field is compensated, as this is not a stable configuration for a zig-zag chain. Instead, the crystal will randomly jump between

the zig and zag configurations due to the potential barrier between them, making the estimation of the peak inherently unreliable (see Fig. 14).

For traps with considerable ratio between the high and low radial frequency modes (denoted as $\omega_h \geq \omega_l$) as our own [31], the sufficient sensitivity for dark ion displacement is achieved in only one radial direction: while ω_l approaches the zig-zag transition frequency, ω_h remains far above it, such that the sensitivity of our measurement is diminished (in our trap, $\omega^{bdb}_{h,\mathrm{COM}} \approx 590\,\mathrm{kHz}$ at the zig-zag transition). As a result, conducting a 2D scan of the bright ion distance vs. the compensation voltages results in a "compensation line", $V_{y'} = mV_{x'} + b$, for which the distance is maximized (see Fig. 15a-b). Following this line of minimal sensitivity, the ion is pushed towards the high radial mode, ω_h. We cannot determine the location of the compensation point along the line from a single 2D scan.

To overcome this obstacle, we exploit the ability to tune the orientation of the radial modes in our trap [31]. By changing the bias voltage V_g, we can change the trap's mode orientation by $\sim 70^\circ$ (see Fig. 15b). This rotation of ω_h and ω_l allows us to find new compensation lines,

$$V_{y'} = m_g V_{x'} + b_g, \tag{33}$$

where m_g and b_g are the linear coefficients for a specific bias voltage, V_g. The intersection of all these lines should give the value of $(V_{x'0}, V_{y'0})$ for which EMM is compensated.

A further complication arises due to the fact that by changing the bias voltage, we also create stray electric fields due to the misalignment of the bias and RF quadrupoles in the trap. This causes a linear dependence of the compensation point on the bias voltage V_g:

$$\begin{aligned} V_{x'g} &= c_{x'} V_g + V_{x'0}, \\ V_{y'g} &= c_{y'} V_g + V_{y'0}. \end{aligned} \tag{34}$$

Here, $(V_{x'g}, V_{y'g})$ are the compensation values for some value of V_g, $(V_{x'0}, V_{y'0})$ are the compensation values for $V_g = 0$, and $(c_{x'}, c_{y'})$ are the linear coefficients, all of which are not known a-priori. Using Eq. 34 to "shift" all compensation lines (Eq. 33) due to the effect of V_g, we get the following set of linear equations:

$$c_{y'} V_g + V_{y'0} = m_g (c_{x'} V_g + V_{x'0}) + b_g. \tag{35}$$

This set of equations has four "free" parameters: $c_{x'}$, $c_{y'}$, $V_{x'0}$, and $V_{y'0}$. Hence, by scanning the 2D compensation voltages for at least four bias voltages, we can extract the compensation points for any value of V_g. The recipe for EMM compensation using a dark ion can be summarized as such:

1. Trap two bright and one dark ions in the bright-dark-bright configuration.

2. Tune the trap RF frequency so that the low radial mode is slightly above the zig-zag transition frequency.

3. Conduct 2D scans of the bright ion distance vs. the compensation voltages, repeating for different bias voltages.

4. Find the linear fit of the resulting compensation lines for each such scan.

5. Solve the linear set of equations described by Eq. 35.

8.2 Estimating the Zig-zag Transition Frequency

Correctly estimating the transition frequency between the linear and zig-zag configurations of the crystal is critical for achieving sufficient sensitivity for the compensation measurements. To derive this transition frequency, let us examine a three-ion crystal in a bright-dark-bright configuration with no external electric field (see Fig. 12). In equilibrium, the forces acting on the bright ions in the axial and radial directions are

$$m_b(\omega_{ax}^b)^2 d = \frac{k_e}{(2d)^2} + \frac{k_e \cos(\theta)}{l^2}, \tag{36}$$

$$m_b(\omega_r^b)^2 x_b = \frac{k_e \sin(\theta)}{l^2}, \tag{37}$$

while the radial forces on the dark ion are equal to

$$m_d(\omega_r^d)^2 x_d = 2\frac{k_e \sin(\theta)}{l^2}. \tag{38}$$

Here, ω_{ax}^b and ω_r^b are the confining frequencies of the bright ions in the axial and radial directions respectively, while ω_r^d is the radial frequency of the dark ion. The masses of the bright and dark ions are similarly denoted as m_b and m_d. $d = d_b/2$ is the axial distance of the bright ions from the trap center. The radial distance of the bright (dark) ion from the trap center is x_b (x_d), where both are taken as positive numbers. From these definitions, the distance between the bright and dark ion, l, and their angle, θ, follows $d = l\cos(\theta)$ and $x_d + x_b = l\sin(\theta)$, as seen in Fig. 12. The Coulomb constant, $k_e = Q^2/4\pi\varepsilon_0$, is defined together with the ions' charges for brevity.

We assume the crystal is nearly linear, and therefore, the angle θ is small ($l \approx d$) such that

$$\tan(\theta) \approx \sin(\theta) \approx \frac{x_d + x_b}{d}, \tag{39}$$

$$\cos(\theta) \approx 1. \tag{40}$$

Under this approximation, from Eq. 36, we get

$$m_b(\omega_{ax}^b)^2 d = \frac{5k_e}{4d^2} \rightarrow \frac{k_e}{d^3} = \frac{4}{5} m_b(\omega_{ax}^b)^2. \tag{41}$$

Inserting this into the radial equations (Eqs. 37 and 38) yields

$$m_b(\omega_r^b)^2 x_b = \frac{k_e(x_d + x_b)}{d^3} = \frac{4}{5} m_b(\omega_{ax}^b)^2 (x_d + x_b), \tag{42}$$

$$m_d(\omega_r^d)^2 x_d = \frac{2k_e(x_d + x_b)}{d^3} = \frac{8}{5} m_b(\omega_{ax}^b)^2 (x_d + x_b). \tag{43}$$

The system transforms to the zig-zag configuration upon the onset of a non-trivial solution ($x_d, x_b \neq 0$) to this set of equations, which gives rise to the following condition:

$$\frac{4}{5} m_b(\omega_{ax}^b)^2 = \frac{m_b(\omega_r^b)^2 \cdot m_d(\omega_r^d)^2}{2m_b(\omega_r^b)^2 + m_d(\omega_r^d)^2}. \tag{44}$$

To further simplify the above expression, we neglect the DC and bias fields effect on the radial trapping frequencies such that

$$m_d(\omega_r^d)^2 = \frac{m_b}{m_d} \cdot m_b(\omega_r^b)^2. \tag{45}$$

Inserting this into Eq. 44, we get the following expression for the critical frequency:

$$\omega_{r,zz}^b \approx \omega_{ax}^b \sqrt{\frac{4}{5}\left(1 + \frac{2m_d}{m_b}\right)}, \tag{46}$$

By relaxing the assumption that the two bright ions have the same radial position and repeating the above linearization, we can get the following eigenvalue equation for the normal mode frequencies (the radial subscript is omitted for brevity):

$$(K - M\omega^2)\bar{x} = 0 \tag{47}$$

where $\bar{x}$ is the ions radial position vector, $M = diag(m_b, m_d, m_b)$ is the ions mass matrix, and the stiffness matrix K is defined as:

$$\begin{pmatrix} m_b\omega_b^2 + \frac{9}{8}\frac{k_e}{d^3} & -\frac{k_e}{d^3} & -\frac{1}{8}\frac{k_e}{d^3} \\ -\frac{k_e}{d^3} & m_d\omega_d^2 + \frac{2k_e}{d^3} & -\frac{k_e}{d^3} \\ -\frac{1}{8}\frac{k_e}{d^3} & -\frac{k_e}{d^3} & m_b\omega_b^2 + \frac{9}{8}\frac{k_e}{d^3} \end{pmatrix} \tag{48}$$

Looking for the approximate center-of-mass (COM) radial-mode frequency, we insert:

$$\bar{x} = (1, 1 + \varepsilon, 1) \tag{49}$$

and find to the leading order in ε that the approximate frequency is a mass weighted average of the confining frequencies:

$$\omega_{COM}^2 \approx \frac{2m_b\omega_b^2 + m_d\omega_d^2}{2m_b + m_d} \tag{50}$$

This expression can be further simplified using eq.45, yielding:

$$\omega_{r,\mathrm{COM}}^{bdb} \approx \omega_r^b \frac{2}{3}\left(1 + \frac{m_b}{2m_d}\right). \tag{51}$$

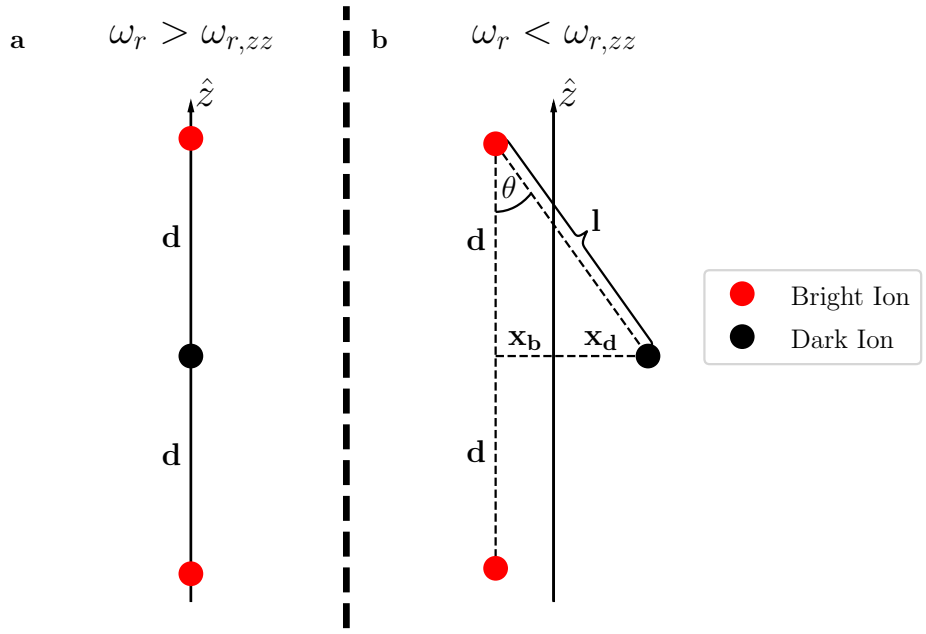

Figure 12: An ion crystal with two bright ions (red circles) and one dark ion (black circle) in the middle. a) Above the zig-zag transition frequency, the ions align in a linear configuration ($x_{b,d} = 0$) at equilibrium. b) Below the zig-zag transition frequency, the equilibrium position of the ions deviates from a straight line ($x_{b,d} > 0$).

8.3 Accounting for the Scattering Force

Along with stray electric fields, an additional source of EMM we need to compensate for is the scattering force due to the cycling transition. We estimate the maximal scattering force on a single bright ion using Eq. 17 at saturation (i.e $s \gg 1$):

$$QE_{sc,\max} = \hbar k\Gamma/2. \tag{52}$$

Here, $\hbar$ is the reduced Planck's constant, $k = 2\pi/\lambda$ is the laser's k-vector with λ the laser wavelength of 397 nm, and $\Gamma \approx 1.36 \times 10^8$ s^{-1} [32] is the transition rate between the $4S_{1/2}$ and the $4P_{1/2}$ states

in $^{40}Ca^{+}$.

In the dark-ion method, the scattering force only affects the bright ions; hence, it deforms the crystal. In this case of uneven forces on the dark and bright ions, we want to calculate the compensation field necessary to make the crystal linear again. In such a case ($x_b = x_d \equiv x$), the radial forces on the bright and dark ions are

$$m_b(\omega_r^b)^2 x = Q(E_r + E_{sc}), \tag{53}$$

$$m_d(\omega_r^d)^2 x = QE_r. \tag{54}$$

Dividing the two above equations, we get, after some rearrangement,

$$E_r = E_{sc} / \left(\frac{m_b(\omega_r^b)^2}{m_d(\omega_r^d)^2} - 1 \right), \tag{55}$$

which can be further simplified using Eq. 45 to

$$E_r \approx E_{sc} / \left(m_d/m_b - 1 \right). \tag{56}$$

This additional source of deformation acts as an effective radial electric field as long as the cycling laser is active, requiring no special attention. The scattering force must be taken into account however, when conducting measurements without the cycling transition being continuously lased, such as spectroscopy measurements involving additional states. In these cases it may be advantageous to work with dark ions which are heavier than the bright ions as opposed to the other way around, due to lighter ions being more tightly confined to the trap center and therefore less susceptible to being affected by the scattering force.

8.4 Sensitivity and Mass Dependence

The dark-ion compensation method relies on the mass difference between ion species, allowing us to measure radial electric fields via the deformation of the Coulomb crystal. In this work, we employed $^{40}Ca^{+}$ and $^{44}Ca^{+}$—the only isotopes that could be consistently ionized and trapped within practical timescales—despite their relatively small 10% mass difference. The sensitivity should be greatly enhanced when co-trapping ion species with a greater mass disparity.

To leading-order, under the influence of a stray radial electric field E_r, the two bright ions will attract each other according to $d_b = 2d_0 - \frac{1}{2}sE_r^2$, where $d_b = 2d$ is the two-bright-ions distance, $d_0 = \left(\frac{5}{4}\frac{k_e}{m_b(\omega_{ax}^b)^2}\right)^{\frac{1}{3}}$ is the bright-ion to center-of-trap distance with no external field as can be recovered from Eq. 41, and s is the dark-ion-method sensitivity,

$$s = -\frac{1}{E_r}\frac{d(d_b)}{dE_r} = -\frac{1}{E_r}\frac{d(d_b)}{d(\Delta x)}\frac{d(\Delta x)}{dE_r}, \tag{57}$$

where $\Delta x = x_d + x_b$ is the bright-to-dark radial distance (see Fig. 12).

We define $\varepsilon = d_0 - d$, where ε is a small ($\varepsilon \ll d, d_0$) axial contraction of the bright ions towards the trap's center. Returning to the axial force equation (Eq. 36) and expanding to second order in $\Delta x/d$, we end up with $\varepsilon = \frac{2}{5}\frac{\Delta x^2}{d_0}$, such that

$$\frac{d(d_b)}{d(\Delta x)} = -2\frac{d\varepsilon}{d(\Delta x)} = -\frac{8}{5}\frac{\Delta x}{d_0}. \tag{58}$$

Adding an external electric-field force, QE_r, to the radial force equations (Eqs. 37 and 38), and expanding to leading order the term $\sin\theta/l^2 \approx \Delta x/d_0^3$, we get

$$\frac{d(\Delta x)}{dE_r} = \frac{Q(m_b(\omega_r^b)^2 - m_d(\omega_r^d)^2)}{m_b(\omega_r^b)^2 m_d(\omega_r^d)^2 - (4/5)m_b(\omega_z^b)^2(2m_b(\omega_r^b)^2 + m_d(\omega_r^d)^2)}. \tag{59}$$

The denominator here corresponds precisely to the zig-zag transition condition (Eq. 44), which is the reason for the sharp increase in sensitivity near the transition point.

For small perturbations, we can approximate $\Delta x \approx \frac{d(\Delta x)}{dE_r}E_r$ in Eq. 58 such that the dark-ion-method sensitivity is given by

$$s = \frac{8}{5d_0}\left(\frac{d(\Delta x)}{dE_r}\right)^2. \tag{60}$$

Fig. 13, shows the sensitivity as a function of the mass ratio m_d/m_b. For a bright ion mass of 40 amu, we fix the axial frequency at $\omega_{ax}^{b,40}/2\pi = 260.4\,\text{kHz}$, same as the measured axial frequency in the system. For other masses, we scale the axial frequency as $\omega_{ax}^{b,m} = \omega_{ax}^{b,40}\sqrt{40/m_b[\text{amu}]}$ thereby keeping the axial trapping field constant. The radial frequency is set to be 5% above the calculated zig-zag transition to ensure that the crystal is in the linear configuration.

To validate the analytical model, we numerically computed the equilibrium positions of the bright ions for various E_r values and fitted the results to extract the sensitivity s. The simulation was based on finding the equilibrium position of the ions by numerically minimizing the potential energy as given by Eqs. 22, 24. The bright ion distance was recorded for different values of E_r, then fitted to a parabola in order to extract the sensitivity per bright-to-dark mass ratio. The numerical results (blue dots in Fig. 13) match the analytical prediction (blue line), confirming the accuracy of the derivation. Note that these calculations are static, i.e. assume zero temperature and thus represent idealized sensitivity.

We note that the sensitivity depends only on the mass ratio between the bright and dark ions, not on their absolute masses. It vanishes when the masses are equal, $m_d/m_b = 1$, and increases as the mass difference grows. The sensitivity function is not symmetric to replacing the roles of bright and dark ions. Higher sensitivity is achieved when the dark ion is the lighter ion, making it advantageous to place the lighter ion in the center of the crystal. On the other hand, heavier dark ions are less tightly

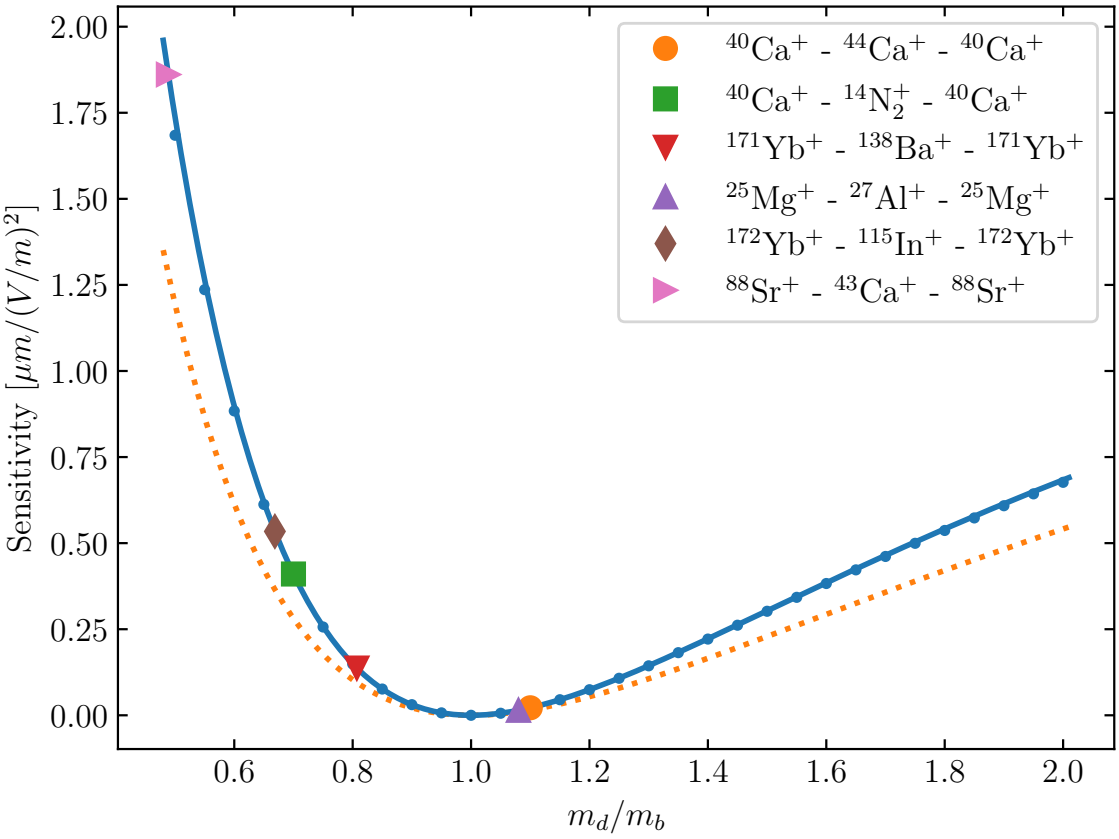

Figure 13: Dark-ion-method sensitivity, $s = -\frac{1}{E_r}\frac{d(d_b)}{dE_r}$. Solid blue line is the result of an analytical calculation (Eq. 60) corroborated by a numerical calculation (blue points). Big markers (see legend) indicate the dark-to-bright mass ratio, m_d/m_b, for different dual-species ion combinations [33–37]. The dotted orange line is the result of the approximation given in Eq. 61. See text for more details on the calculation parameters.

bound, causing the crystal to be more deformed due to the scattering force. Hence, in mixed-species experiments where both ions can be imaged by laser fluorescence, placing the lighter ion in the middle increases precision at the cost of accuracy while a heavier dark ion does the inverse.

To further simplify the sensitivity expression, we use the approximation given in Eq. 45. With this approximation, the sensitivity takes a simple form,

$$s = \frac{8Q^2}{5d_0 m_b^4}\left(\frac{m_d - m_b}{(\omega_r^b)^2 - (\omega_{r,zz}^b)^2}\right)^2. \tag{61}$$

Here, we see the sensitivity scaling with the radial bending frequency, $s \propto (\omega_{r,\text{bend}}^{bdb})^{-4}$, as $\omega_{r,\text{bend}}^{bdb} \approx \sqrt{(\omega_r^b)^2 - (\omega_{r,zz}^b)^2}$. A comparison between the exact solution (Eq. 60) and this approximation is shown in Fig. 13. Under the condition that the radial frequency, ω_r^b, is a multiplicative factor (e.g., 5% above) of the transition to zig-zag frequency, $\omega_{r,zz}^b$, we get that the sensitivity scales as $(\omega_{ax}^b)^{-4}$.

This emphasizes that the method is more sensitive at lower axial trapping frequencies.

8.5 Compensation Results

Throughout the compensation measurements, we fixed the axial frequency of a single bright ion in the trap to $\omega_{ax}^{b}/2\pi = 260.4\,\text{kHz}$. Using equation Eq. 51, we can estimate the linear to zig-zag transition frequency in terms of the crystal's COM mode to be $\omega_{r,zz}^{bdb}/2\pi = 404\,\text{kHz}$.

The dependence of the distance between the bright ions on the EMM and the low radial-mode frequency is shown in Fig. 14. We vary the compensation voltages, $V_{\perp} = f(V_{x'}, V_{y'})$, to create a field along the direction of the low-frequency mode, ω_l, and record the bright-ions positions. Here, f is a linear function of the compensation-electrodes voltage, which we found experimentally (the line orthogonal to the purple line in Fig. 15c as we performed the experiment with a bias voltage $V_g = 0.6\,\text{V}$). We repeat this procedure for different radial-mode trapping frequencies. The value of the crystal COM mode, $\omega_{l,\text{COM}}^{bdb}$, was found using the "tickle" method [6]. As the low radial mode frequency approaches the zig-zag transition frequency, the point where the crystal is at its maximal extent becomes increasingly pronounced due to the higher sensitivity. When the frequency dips below its critical value however, the crystal "jumps" over the maximal extent, distorting the shape of the bright ion distance curve. While this effect is barely noticeable near the transition frequency, it becomes increasingly pronounced as the confinement is reduced and the gap between the zig and zag configurations increases.

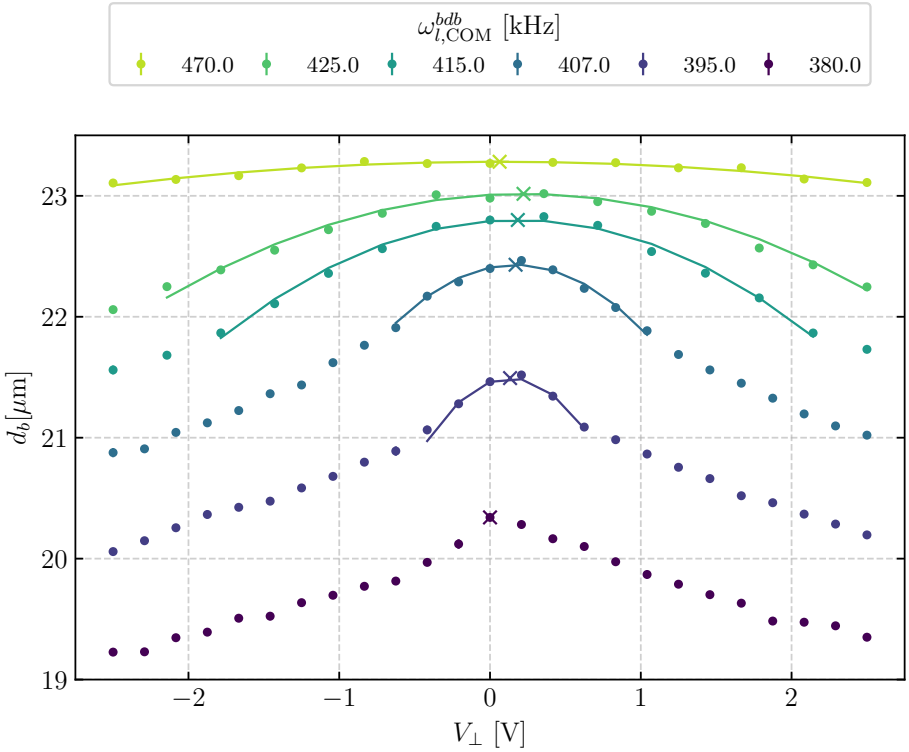

Figure 14: Bright ion separation, d_b, as function of an applied radial electric field for different low radial mode frequencies, $\omega^{bdb}_{l,\mathrm{COM}}$ (legend). The electric field is applied along the direction of the low radial mode. The trap is compensated (not necessarily at the x-axis origin) when the distance between the bright ions is at its maximum. We extract the compensation value via a local parabola fit to the data (solid lines, cross indicate fit maximum). The measurement peak becomes more pronounced, and the range of quadratic dependence narrows as the radial frequency approaches the transition to zig-zag. Below the transition frequency to zig-zag ($\sim 404\,\mathrm{kHz}$), bright ions display a noticeable discontinuity in their positions as the crystal jumps between the zig and zag configurations, with the bright ion distance no longer fitting a parabola when looking far below the transition frequency.

The results of the compensation procedure detailed in section 8.1 for six different bias voltages are shown in Fig. 15c. The 2D compensation scans were performed with the low-radial mode frequency set to $\omega^{bdb}_{l,COM}/2\pi = 430\,\mathrm{kHz}$ so as to avoid the possibility of it drifting below the zig-zag transition frequency mid-measurement. The compensation lines in Fig. 15c are shifted by the estimated correction due to the bias voltage, allowing us to clearly see their intersection at the $V_g = 0$ compensation point.

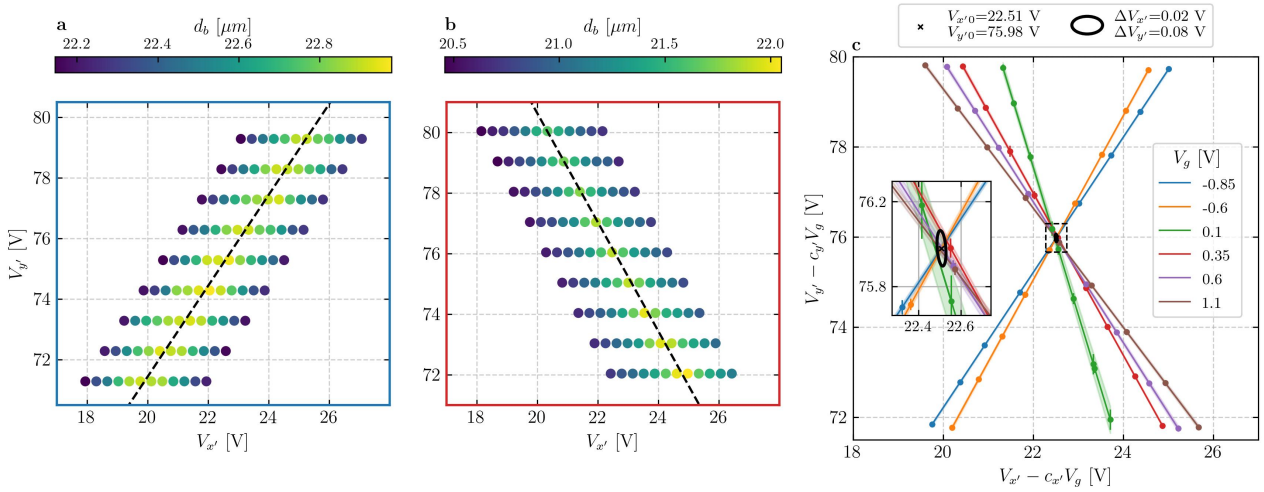

Figure 15: Dark ion EMM compensation. a-b) Bright ion distance (color scale) as a function of the compensation voltages $(V_{x'}, V_{y'})$ for different bias voltages (a) $V_g = -0.85\,\mathrm{V}$, b) $V_g = 0.35\,\mathrm{V}$). Throughout the measurements, we kept the low-radial mode frequency at $\omega_{l,\mathrm{COM}}^{bdb} = 430\,\mathrm{kHz}$ to avoid accidentally crossing the zig-zag transition frequency mid-measurement. The maximal ion distance follows a linear line in $(V_{x'}, V_{y'})$ space (dashed black line), the angle of which is determined by the radial-modes orientation. These lines are identical to those in (c) for bias voltages, $V_g = -0.85\,\mathrm{V}$ (blue) and $V_g = 0.35\,\mathrm{V}$ (red), as denoted by the color of the frames. c) Compensation lines for different bias voltages (see legend). Each line is a linear fit as in (a-b), the points being the peaks of the ion distances found for each $V_{y'}$ in the 2D scans. The lines are shifted by the dependence of the compensation point on V_g (Eq. 34), so they all intersect at a single point ($c_{x'} = -0.23 \pm 0.07$, $c_{y'} = 0.57 \pm 0.04$). The ellipse shows the one-sigma error in the estimation of $(V_{x'0}, V_{y'0})$.

The resulting uncertainty of $\Delta V \approx 0.1\,\mathrm{V}$ in the compensation voltages was estimated to correspond to a stray electric field uncertainty of $\Delta E_r \approx 0.2\,\mathrm{V\,m^{-1}}$ [1]. This uncertainty is at a level consistent with the uncompensated stray-field magnitudes reported in typical ion-trap experiments, and was accomplished despite the sensitivity of the measurements not being fully maximized. In order to verify our results, the estimated compensation voltages were compared between this method and one using only a single bright ion [1, 16], whose details lie outside the scope of this thesis. The results of this comparison are shown in Fig. 16. While the two methods yield similar compensation uncertainties, there is a small discrepancy between them, which cannot be attributed to random error. As the results of the single-ion compensation are consistent before and after the dark-ion measurement, we can rule out drifts as the cause of the discrepancy.

One possible systematic effect that differentiates between the two schemes is the presence of the scattering force from the fluorescence laser during the measurements, as explained in section 8.3. The scattering force acts as an additional effective stray field in the bright-ion scheme (on saturation,

the maximal scattering field is $E_{sc,\max} \approx 0.7\,\mathrm{V\,m^{-1}}$). To compensate for the effect of the scattering force, we need to apply an equal and antiparallel field, $E_r = -E_{sc}$, in the single bright ion method. In contrast, in the dark-ion scheme, the scattering force acts only on the bright ions, where the dark ion is unaffected by the scattering force, causing additional deformation in the crystal. To compensate for this deformation, we need to apply a compensation field $E_r \approx E_{sc}/(m_d/m_b - 1)$. This amounts to $E_r \approx 10E_{sc}$ for our bright and dark ion masses. From the above discussion and the comparison made in Fig. 16, we can give an upper bound to the scattering field in our experiment to be $E_{sc} \lesssim 0.1\,\mathrm{V\,m^{-1}}$.

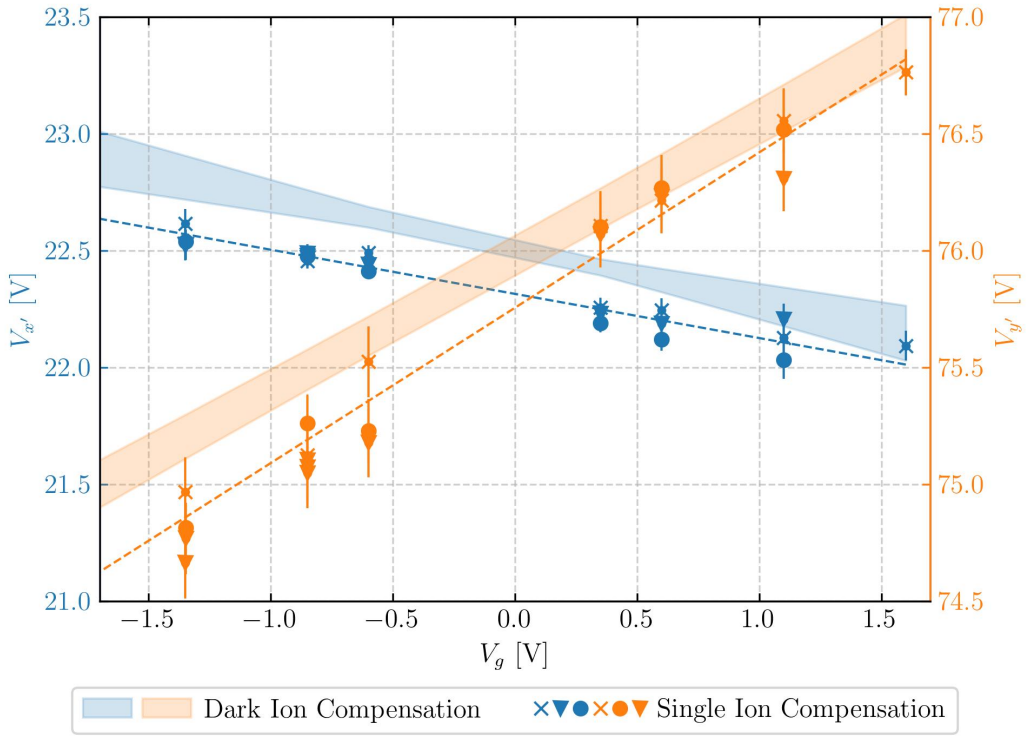

Figure 16: Comparison between the single ion (markers) and dark ion (shaded areas) compensation methods. The estimated $V_{x'}$ (blue, left y-axis) and $V_{y'}$ (orange, right y-axis) compensation voltages are shown as a function of the bias voltage V_g. Markers symbols corresponds to single-ion experiments performed before (cross) and after (circle, triangle) the dark-ion experiment.

While most EMM compensation schemes are performed for each bias voltage independently, the dark-ion scheme requires several measurements for different bias voltages, resulting in a linear fit for the EMM compensation as a function of the bias voltage. This is due to the sensitivity scaling in the dark-ion method. Since we rely on axial contraction as an indicator of a radial field, the sensitivity scales as (see section 8.4):

$$\frac{1}{E_r}\frac{d(d_b)}{dE_r} \propto (\omega^{bdb}_{r,\mathrm{bend}})^{-4} \tag{62}$$

where $\omega^{bdb}_{r,\mathrm{bend}}$ is the frequency of the bending radial mode, where the two bright ions move out of phase

with respect to the dark. This mode approaches zero when approaching the zig-zag transition point, requiring us to work close to it in order to enhance the sensitivity. Our trap has a large low-to-high radial frequency ratio ($\omega_l/\omega_h \approx 0.7$), limiting our sensitivity in the high radial mode direction while the low radial mode is kept above the zig-zag transition. For more symmetric traps ($\omega_l \sim \omega_h$), it should be possible to simultaneously compensate EMM in the two radial directions in a single scan at a specific bias voltage. Such a scenario would make the dark-ion method significantly more attractive, as it would reduce its time requirement to a few minutes instead of close to an hour. Unfortunately, our setup cannot meet these symmetric conditions, so these claims cannot be experimentally verified at this time.

9 Discussion

In this thesis, we built a functioning ion trap for trapping, cooling and imaging calcium ions, as well as implemented two important diagnostic techniques for the system. Both of these techniques rely on using Coulomb crystals composed of a mix of two calcium isotopes, and exploiting their differing characteristics.

The first technique was the development and calibration of an ion-shuffling pressure gauge, which enables pressure estimation at the exact ion location. The gauge relies on the shift in energy levels between the isotopes, creating visually distinguishable bright and dark (fluorescing and non-fluorescing) ions, and was used to estimate the final system pressure to be in the low 10^{-11} mbar range.

In addition, we devised and demonstrated an entirely novel method for the detection and compensation of stray electric fields using a dark ion embedded between two bright ions [1]. This dark ion compensation scheme uses the differing radial confinement of the two ion types, thus evaluating the external field from the difference in their response. The sensitivity of this technique was sufficiently enhanced to achieve a compensation level comparable to that of typical ion trapping experiments, in the timescale of tens of minutes.

Both of these techniques are relatively simple in concept, and readily accessible to the majority of ion trapping systems. In particular, the dark ion EMM compensation method has the distinct advantage over many competing techniques in that it allows for compensating in both radial directions while requiring only the ability to image the fluorescing ions in the axial direction. The rising interest in multi-species ion crystals should make the method particularly attractive, as it can be seamlessly included in experiments which already involve differently massed ions.

The work described in this thesis serves as a a solid foundation for future experiments involving the co-trapping and control of atomic and molecular ions. The system has already been used to co-trap Ca^+ and N_2^+ as well as conduct simple spectroscopy measurements.

References

[1] O. Barnea, D. Einav, J. Drotleff, I. Hochner, and Z. Meir, "Micromotion compensation using dark and bright ion species," Frontiers in Quantum Science and Technology **4**, 1596801 (2025).

[2] P. O. Schmidt, T. Rosenband, C. Langer, W. M. Itano, J. C. Bergquist, and D. J. Wineland, "Spectroscopy Using Quantum Logic," Science **309**, 749–752 (2005).

[3] H. S. Margolis, "Optical frequency standards and clocks," Contemporary Physics **51**, 37–58 (2010).

[4] J. I. Cirac and P. Zoller, "Quantum computations with cold trapped ions," Phys. Rev. Lett. **74**, 4091–4094 (1995).

[5] C. D. Bruzewicz, J. Chiaverini, R. McConnell, and J. M. Sage, "Trapped-ion quantum computing: progress and challenges," Applied Physics Reviews **6**, 021314 (2019).

[6] M. Drewsen, A. Mortensen, R. Martinussen, P. Staanum, and J. L. Sørensen, "Nondestructive identification of cold and extremely localized single molecular ions," Physical Review Letters **93** (2004).

[7] A. Mokhberi and S. Willitsch, "Structural and energetic properties of molecular coulomb crystals in a surface-electrode ion trap," New Journal of Physics **17**, 045008 (2015).

[8] M. Sinhal, Z. Meir, K. Najafian, G. Hegi, and S. Willitsch, "Quantum-nondemolition state detection and spectroscopy of single trapped molecules," Science **367**, 1213–1218 (2020).

[9] D. Holzapfel, F. Schmid, N. Schwegler, O. Stadler, M. Stadler, A. Ferk, J. P. Home, and D. Kienzler, "Quantum control of a single H_2^+ molecular ion," Phys. Rev. X **15**, 031009 (2025).

[10] Y. Lin, D. R. Leibrandt, D. Leibfried, S. M. Brewer, D. J. Wineland, D. B. Hume, T. R. Tan, C. Kurz, D. R. Crick, C. H. Christensen, and T. Rosenband, "Quantum entanglement between an atom and a molecule," Nature **581**, 273–277 (2020).

[11] Y. Aikyo, G. Vrijsen, T. W. Noel, A. Kato, M. K. Ivory, and J. Kim, "Vacuum characterization of a compact room-temperature trapped ion system," Applied Physics Letters **117**, 10.1063/5.0029236 (2020).

[12] A. M. Hankin, E. R. Clements, Y. Huang, S. M. Brewer, J.-S. Chen, C. W. Chou, D. B. Hume, and D. R. Leibrandt, "Systematic uncertainty due to background-gas collisions in trapped-ion optical clocks," Phys. Rev. A **100**, 033419 (2019).

[13] D. J. Berkeland, J. D. Miller, J. C. Bergquist, W. M. Itano, and D. J. Wineland, "Minimization of ion micromotion in a paul trap," Journal of Applied Physics **83**, 5025–5033 (1998).

[14] J. Keller, H. L. Partner, T. Burgermeister, and T. E. Mehlstäubler, "Precise determination of micromotion for trapped-ion optical clocks," Journal of Applied Physics **118**, 104501 (2015).

[15] T. F. Gloger, P. Kaufmann, D. Kaufmann, M. T. Baig, T. Collath, M. Johanning, and C. Wunderlich, "Ion-trajectory analysis for micromotion minimization and the measurement of small forces," Phys. Rev. A **92**, 043421 (2015).

[16] R. Saito, K. Saito, and T. Mukaiyama, "Measurement of ion displacement via rf power variation for excess micromotion compensation," Journal of Applied Physics **129**, 124302 (2021).

[17] F. Wolf, Y. Wan, J. C. Heip, F. Gebert, C. Shi, and P. O. Schmidt, "Non-destructive state detection for quantum logic spectroscopy of molecular ions," Nature **530**, 457–460 (2016).

[18] E. Madge, G. Perez, and Z. Meir, "Prospects of nuclear-coupled-dark-matter detection via correlation spectroscopy of I_2^+ and Ca^+," Phys. Rev. D **110**, 015008 (2024).

[19] T. Levin and Z. Meir, "Coherent dynamics of a nuclear-spin-isomer superposition," Phys. Rev. Res. **7**, 013274 (2025).

[20] S. Earnshaw, "On the nature of the molecular forces which regulate the constitution of the luminiferous ether," Transactions of the Cambridge Philosophical Society (1842).

[21] D. J. Wineland, C. Monroe, W. M. Itano, D. Leibfried, B. E. King, and D. M. Meekhof, "Experimental Issues in Coherent Quantum-state Manipulation of Trapped Atomic Ions," J. Res. Natl. Inst. Stand. Technol. **103**, 259–328 (1998).

[22] D. L. D. Leibfried, "Trapping and cooling of atomic ions," in *Ion traps for tomorrow's applications*, Vol. 189, Proceedings of the International School of Physics "Enrico Fermi" (IOS Press, Amsterdam, 2015), pp. 1–63.

[23] M. Ramm, T. Pruttivarasin, M. Kokish, I. Talukdar, and H. Häffner, "Precision measurement method for branching fractions of excited $P_{1/2}$ states applied to $^{40}Ca^+$," Phys. Rev. Lett. **111**, 023004 (2013).

[24] D. Leibfried, R. Blatt, C. Monroe, and D. Wineland, "Quantum dynamics of single trapped ions," Rev. Mod. Phys. **75**, 281–324 (2003).

[25]D. James, "Quantum dynamics of cold trapped ions with application to quantum computation," Applied Physics B: Lasers and Optics **66**, 181–190 (1998).

[26]M. Bernardini, S. Braccini, R. De Salvo, A. Di Virgilio, A. Gaddi, A. Gennai, G. Genuini, A. Giazotto, G. Losurdo, H. B. Pan, A. Pasqualetti, D. Passuello, P. Popolizio, F. Raffaelli, G. Torelli, Z. Zhang, C. Bradaschia, R. Del Fabbro, I. Ferrante, F. Fidecaro, P. La Penna, S. Mancini, R. Poggiani, P. Narducci, A. Solina, and R. Valentini, "Air bake-out to reduce hydrogen outgassing from stainless steel," Journal of Vacuum Science & Technology A **16**, 188–193 (1998).

[27]A. Kramida, Y. Ralchenko, J. Reader, and N. A. Team, *Nist atomic spectra database (version 5.11)*, https://physics.nist.gov/asd, 2023.

[28]D. M. Lucas, A. Ramos, J. P. Home, M. J. McDonnell, S. Nakayama, J.-P. Stacey, S. C. Webster, D. N. Stacey, and A. M. Steane, "Isotope-selective photoionization for calcium ion trapping," Phys. Rev. A **69**, 012711 (2004).

[29]H. Kaufmann, S. Ulm, G. Jacob, U. Poschinger, H. Landa, A. Retzker, M. B. Plenio, and F. Schmidt-Kaler, "Precise experimental investigation of eigenmodes in a planar ion crystal," Phys. Rev. Lett. **109**, 263003 (2012).

[30]S. Fishman, G. De Chiara, T. Calarco, and G. Morigi, "Structural phase transitions in low-dimensional ion crystals," Phys. Rev. B **77**, 064111 (2008).

[31]R. Saito and T. Mukaiyama, "Determination of principal axes orientation in an ion trap using matter-wave interference," Opt. Express **32**, 42616–42623 (2024).

[32]P. Barakhshan, A. Marrs, A. Bhosale, B. Arora, R. Eigenmann, and M. S. Safronova, *Portal for High-Precision Atomic Data and Computation* (version 2.0). University of Delaware, Newark, DE, USA. URL: https://www.udel.edu/atom [February 2022].

[33]M. Sinhal, Z. Meir, K. Najafian, G. Hegi, and S. Willitsch, "Quantum-nondemolition state detection and spectroscopy of single trapped molecules," Science **367**, 1213–1218 (2020).

[34]J. M. Pino, J. M. Dreiling, C. Figgatt, J. P. Gaebler, S. A. Moses, M. Allman, C. Baldwin, M. Foss-Feig, D. Hayes, K. Mayer, et al., "Demonstration of the trapped-ion quantum ccd computer architecture," Nature **592**, 209–213 (2021).

[35]S. M. Brewer, J. S. Chen, A. M. Hankin, E. R. Clements, C. W. Chou, D. J. Wineland, D. B. Hume, and D. R. Leibrandt, "$^{27}Al^{+}$ Quantum-Logic Clock with a Systematic Uncertainty below 10^{-18}," Physical Review Letters **123**, 033201 (2019).

[36]H. N. Hausser, J. Keller, T. Nordmann, N. M. Bhatt, J. Kiethe, H. Liu, I. M. Richter, M. von Boehn, J. Rahm, S. Weyers, E. Benkler, B. Lipphardt, S. Dörscher, K. Stahl, J. Klose, C. Lisdat, M. Filzinger, N. Huntemann, E. Peik, and T. E. Mehlstäubler, "$^{115}In^{+}$—$^{172}Yb^{+}$ Coulomb Crystal Clock with 2.5×10^{-18} Systematic Uncertainty," Phys. Rev. Lett. **134**, 023201 (2025).

[37]A. C. Hughes, V. M. Schäfer, K. Thirumalai, D. P. Nadlinger, S. R. Woodrow, D. M. Lucas, and C. J. Ballance, "Benchmarking a high-fidelity mixed-species entangling gate," Phys. Rev. Lett. **125**, 080504 (2020).